Journal of the Brazilian Society of Mechanical Sciences and Engineering (2024) 46:333
https://doi.org/10.1007/s40430-024-04905-y

TECHNICAL PAPER

Lattice Boltzmann method for simulating transport phenomena avoiding the use of lattice units

Ivan T. Martins[1] · Pablo F. Alvariño[2] · Luben Cabezas-Gómez[1]

Received: 25 May 2023 / Accepted: 8 April 2024

Abstract
In this paper, we propose a dimensional lattice Boltzmann method (LBM) that numerically solves the discrete lattice Boltzmann equation directly in physical units. This procedure facilitates the LBM application for simulating transport phenomena completely avoiding the use of lattice units and consequently of any particular unit conversion system. Several test problems related to different physical phenomena are simulated, such as heat diffusion, lid-driven cavity, forced convection in channels (both developed and under development) and two-phase liquid–gas systems, considering stationary and dynamic flows under very high density and viscosity ratios. We compare the numerical results with analytical or finite difference solutions, finding a good agreement between them. Similarly, we performed a stability analyses for three of the test cases. The traditional LBM was also considered for the sake of comparison, showing both the same accuracy and stability, as expected. Furthermore, we present solutions using the Allen–Cahn phase-field LBM model for high liquid/gas density and gas/liquid kinematic viscosity ratios, up to 43,300 and 470, respectively, commonly not found in open literature. The proposed methodology enhances the LBM use as a simulation tool for the wide transport phenomena where it finds application.

Keywords Dimensional LBM · LBM without lattice units · Transport phenomena simulation · Modified LBE for physical units

1 Introduction

Nowadays, the lattice Boltzmann method (LBM) has been extensively used to simulate a wide range of transport phenomena. A set of examples is: fluid flow and heat transfer [12] problems, flows in porous media [36, 54, 78], heat transfer with nanofluids [37, 73, 81, 82], multiphase flows with liquid-liquid or liquid–gas systems [66, 71, 76, 83], thermal phase-change phenomena, both liquid–gas and solid–liquid [15, 35, 48, 58, 68, 72] and many others that could be mentioned here. These transport phenomena are of great importance for diverse engineering applications considering petroleum, energy, nuclear, electronic and refrigeration industries, to name a few.

The LBM is a mesoscopic method that is based on the numerical solution of the discrete Boltzmann transport equation in phase space and time, called the lattice Boltzmann equation (LBE). The LBE was first proposed by McNamara and Zanetti [56] and is used to numerically find the values of particle distribution functions over the discrete domain. Then, macroscopic fields (such as density, velocity, concentration, temperature and others) can be calculated from the statistical moments of these functions [38, 56, 75]. The LBM allows recovering the macroscopic conservative laws through an asymptotic analysis called the Chapman–Enskog analysis [10]. This fact confirms that we can recover the macroscopic behavior of a physical system by the numerical solution of the LBE, which represents the mesoscopic level of the physical phenomena, as proven in Wolf-Gladrow [80].

Technical Editor: Francis HR Franca.

✉ Ivan T. Martins
ivanmartins@usp.br

Pablo F. Alvariño
pablo.farinas@udc.es

Luben Cabezas-Gómez
lubencg@sc.usp.br

[1] Heat Transfer Research Group, Department of Mechanical Engineering, São Carlos School of Engineering (EESC), University of São Paulo (USP), São Carlos, São Paulo 13566-590, Brazil

[2] University of A Coruña, Ferrol Industrial Campus, 15403 Ferrol, A Coruña, Spain

Published online: 05 May 2024

Traditionally, the LBM is solved in so-called lattice units (lu) or lattice scales, which generally consider unitary spatial and temporal increments. There are two main methods employed to establish the relationships between physical and lattice scales. The first is the dimensional analysis, based on the use of Buckingham's Π theorem, first proposed by Buckingham [8]. The second is the scaling method (or principle of corresponding states), which makes use of the thermodynamic equations of state (EoS) [2, 31]. The Π theorem is commonly applied to infer dimensionless groups (Π) from the units of the input variables in the absence of known governing equations [3]. Once the governing equations are established, performing scale analysis through the non-dimensionalization process allows the identification of representative dimensionless numbers. This process also helps to find the coefficients of the equation in terms of specific references to the variables of the problem [3]. These references must be known and constant [2].

Several works have proposed different approaches for unit conversion in LBM. See for example the following works, to name a few of them, [2, 30, 31, 38, 74, 79]. In general, a set of works uses the Buckingham Π theorem to relate the physical scale with the lattice scale [30], generally to solve some multiphase flows problems. Other authors [74] used only the scale analysis, to find the main dimensionless numbers and simulate melting and solidification processes. As pointed out by Baakeem et al. [2], we can also make use of the Buckingham Π theorem and scale analysis together. This allows properties such as specific heat capacity, viscosity and thermal diffusivity, which do not have a reference state, to be considered in the conversion process. In a recent study, [31] proposed the use of Planck units as a reference for performing the conversion between physical and lattice units, respectively. The method was successfully applied to simulate forced convection in tube banks considering heat sources, but required more steps in the unit conversion process.

Baakeem et al. [2] proposed a general procedure for simulating several fluid flow and heat transfer problems, including a two-dimensional stationary droplet with the pseudopotential model. The procedure is based on using the same basic reference parameters of the physical scale and the lattice scale to carry out the conversion process. The methodology allows certain flexibility while guaranteeing the stability of the solution. Very recently Wang et al. [79] developed a conversion strategy to simulate liquid–vapor phase change with the pseudopotential method. The authors proposed conversion relations for the fundamental units using the surface tension and EoS parameters related to fluid properties, in order to deduce conversion relations of other quantities. They also simulated a single bubble nucleation process by recovering the latent heat of the fluid and the correct superheating temperature in physical units.

However, the use of any non-dimensionalization procedure implies the addition of some computational steps before starting to simulate the problem. This also adds more calculations for post-processing the output simulated data. The procedures require, in fact, a carefully analysis that depends of each specific problem solved, having a certain degree of complexity. Cates et al. [9] simulated binary fluid mixtures in the presence of colloid particles and stated that LBM cannot completely resolve the hierarchy of length, energy and time-scales that arise in typical flows of complex fluids. Thus, it had to be decided which physics to solve and what to leave unsolved when colloidal particles were present in one or both phases of the fluid. Therefore, it is very important to choose the most relevant dimensionless numbers for an adequate simulation of the macroscopic problem.

The procedure is applied to solve five problems: involving one-dimensional heat conduction with heat source; two-dimensional lid-driven cavity; heat transfer by convection in a two-dimensional channel, considering developed and developing flow, both with constant and oscillating heat flux; the two-phase problem of a static bubble surrounded by liquid (air-water and liquid–vapor of saturated water systems) and the solution of the dynamic layered Poiseuille flow for the same two-phase systems considered for the static problem. We adopted the phase-field LBM model based on the conservative Allen–Cahn equation to solve multiphase problems, after its modification to the dimensional approach. In addition, we also present the solutions to three other classic problems in Appendices 1, 2 and 3. All numerical results are compared with reference solutions considering both the proposed and traditional LBM (solved in lattice units). These reference solutions are analytical when available, based on benchmark solutions from the literature or calculated using the finite difference method. A stability analysis was also carried out for three of the problems mentioned, aiming to compare the dimensional and conventional models.

The rationale for the proposed method was the use of traditional LBM established to simulate real problems, but employing physical units directly throughout the solution of the problem. This was also motivated by the need to simulate practical problems in their real conditions (thermophysical properties, domain geometry, numerical size refinement and others). Commonly, the use of traditional LBM is followed by the implementation of a set of dimensionless numbers which are sometimes not entirely correct. For example, a density ratio is used for a specific two-phase fluid system, but the dimensionless surface tension considered does not correspond to the actual fluid considered in the simulation. This issue is addressed in Sects. 3.4 and 3.5 of the paper. The authors noted that the solved LBE preserves the physical dimensionality if all variables are used in physical units,

including time and spatial increments. Then, through the simulation of several test problems, they verified the correctness and validity of the solutions obtained and of the entire procedure.

The main novelty of the paper is the proposition of dimensional LBM, which is a version of traditional LBM that performs all calculations in physical units, facilitating the application of the method. In this context, the specific novelties are: (I) proposition of dimensional LBM for two collision operators (BGK and MRT). Note that modifying the dimensionless MRT operator to the dimensional one is non-trivial; (II) modification of the traditional formulation of boundary conditions for direct use in physical units (see Eq. 21); (III) solution of hydrodynamic two-phase problems with a phase-field LBM based on the Allen–Cahn equation and proposition of a dimensional version of this LBM model and (IV) exploration of this phase-field LBM model in regions with high density and viscosity ratios, not previously published in the open literature.

The paper is divided into four main sections: In Sect. 2 is presented the proposed dimensional LBM, while the results and the conclusions are provided in Sects. 3 and 4, respectively.

2 The dimensional LBM

It is common in LBM to consider variables in lattice units rather than physical units [38, 59, 75]. This requires the use of dimensionless numbers to represent all physical parameters. The non-dimensionalization process generally involves choosing reference unit scales, which are defined by independent conversion factors and by the employment of similarity laws, in order to obtain the dimensionless values of all physical variables of the problem [38]. There are several methods in the literature to perform this non-dimensionalization process, as well as to map the physical properties of a specific system to the lattice scales (and vice-versa). Some of these methods are presented by Su and Davidson [74], Huang et al. [31], Baakeem et al. [2] and Wang et al. [79]. These works give an idea of the complexity embraced in this unit conversion process, which is greater for the simulation of multiphase and multicomponent problems.

To distinguish between the LBM proposed in this paper and the traditional LBM, which relies on a non-dimensionalization process, we refer to the former as the "dimensional LBM" and the latter as the "conventional LBM". The dimensional LBM involves applying the LBM in its dimensional form. This means that the non-dimensionalization process is not applied, and the values of Δx, Δt, $c = \Delta x/\Delta t$ and all macroscopic variables (density, velocity, temperature, viscosity and others) are used in physical units, preferably in the SI unit system. This approach completely eliminates the need for unit conversion procedures, which are typically employed for: map physical units of input data into lattice units, perform numerical simulations in lattice units and then map the output data from the lattice space back to the physical domain. Therefore, there is no need to select or employ any conversion parameters. Additionally, the entire simulation, including data input and output, is performed in physical units. A schematic representation of the dimensional LBM procedure is shown in Fig. 1, in comparison with the traditional procedure.

In the following sections, we present the dimensional LBM models. The lattice Boltzmann equations (LBEs) of these models have been appropriately modified by incorporating Δt, Δx and c when necessary, to ensure that all variables are utilized in physical units during the simulations.

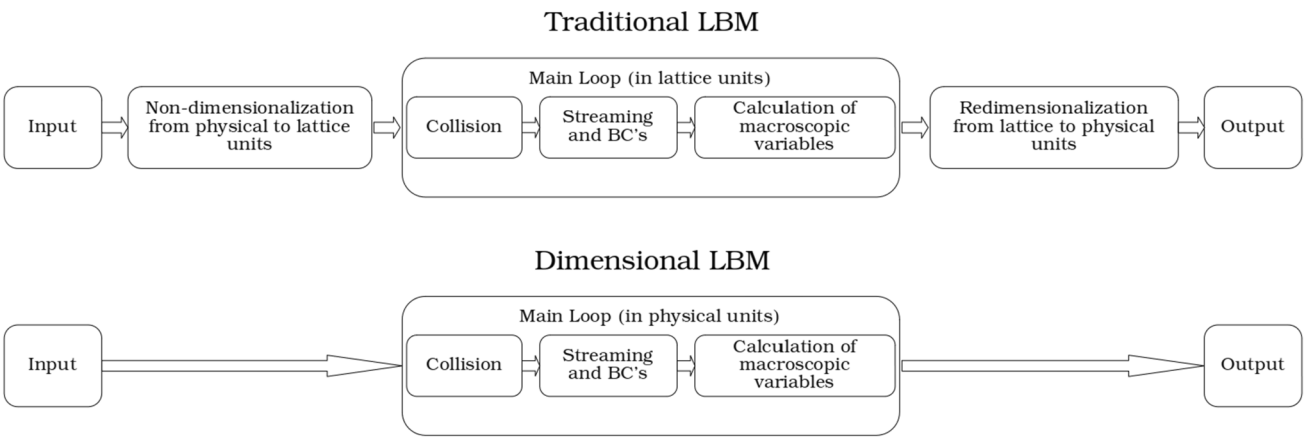

Fig. 1 Schematic representation of the dimensional LBM procedure

2.1 Dimensional LBM for fluid flow

The LBM is founded on the discretization of the Boltzmann transport equation within the phase space defined by velocity, physical space and time [38]. This discretization process yields the discrete LBE, which serves as the equation solved numerically. Considering a second-order discretization in time, a general form of the LBE can be given by Eq. 1. This equation delineates the evolution of the discrete distribution functions, f_i, in both space and time for each discrete velocity direction i.

$$f_i(\mathbf{x}+\mathbf{c_i}\Delta t, t+\Delta t) - f_i(\mathbf{x},t) = \Delta t\left[\Omega_i(\mathbf{x},t) + S_{f_i}(\mathbf{x},t)\right]. \tag{1}$$

In Eq. 1, S_{f_i} represents the source term associated with external forces, particularly in fluid motion simulations. Here, Δt and Δx denote the discrete time and space intervals, respectively, while $\mathbf{c_i}$ represents the discrete particle velocities in each i direction. Typically, velocity schemes are defined as DdQq, following [62], where d represents the spatial dimension of the simulation (one, two or three-dimensional) and q is the number of discrete velocities considered.

The variable Ω_i of Eq. 1 represents the collision operator, which accounts for particle collisions. This operator can be modeled in various forms. The simplest form that enables the simulation of Navier–Stokes equations (NSE) is the Bhatnagar–Gross–Krook (BGK) collision operator [6], defined as: $\Omega_i^{\mathrm{BGK}} = -(f_i - f_i^{\mathrm{eq}})/\tau$, where τ denotes the relaxation time and f_i^{eq} is the equilibrium distribution function, representing the system's state at equilibrium. With the BGK operator in mind, the LBE can be rewritten as presented in Eq. 2.

$$f_i(\mathbf{x}+\mathbf{c_i}\Delta t, t+\Delta t) - f_i(\mathbf{x},t) = -\frac{\Delta t}{\tau}\left[f_i(\mathbf{x},t) - f_i^{\mathrm{eq}}(\mathbf{x},t)\right] + S_{f_i}(\mathbf{x},t)\Delta t. \tag{2}$$

The equilibrium distribution function, f_i^{eq}, is determined by Eq. 3 [23, 38], which is applicable for the slightly compressible NSE. In this equation, ρ denotes the fluid density, c_s represents the lattice sound speed and w_i are the weights for each velocity direction i. The values of c_s and w_i also depend on the selected velocity scheme.

$$f_i^{\mathrm{eq}}(\mathbf{x},t) = w_i\rho(\mathbf{x},t)\left[1 + \frac{\mathbf{c}_i\cdot\mathbf{u}}{c_s^2} + \frac{(\mathbf{c}_i\cdot\mathbf{u})^2}{2c_s^4} - \frac{\mathbf{u}\cdot\mathbf{u}}{2c_s^2}\right]_{(\mathbf{x},t)}. \tag{3}$$

For the two-dimensional $D2Q9$ velocity scheme, $c_s = c/\sqrt{3}$. The velocities and weights are defined by Eqs. 4 and 5 [62]. The variable c accounts for the lattice speed, defined as $c = \Delta x/\Delta t$.

$$\mathbf{c_i} = c\begin{cases}(0,0), & i=0,\\ (1,0),(0,1),(-1,0),(0,-1), & i=1,\ldots,4,\\ (1,1),(-1,1),(-1,-1),(1,-1), & i=5,\ldots,8.\end{cases} \tag{4}$$

$$w_i = \begin{cases}4/9, & i=0,\\ 1/9, & i=1,\ldots,4,\\ 1/36 & i=5,\ldots,8.\end{cases} \tag{5}$$

It is important to note that through Chapman–Enskog analysis [10], we can recover the NSE with sufficient degree of precision, establishing a direct connection between the LBE and the NSE. This connection is expressed by the relationship between the relaxation time τ and the fluid's kinematic viscosity ν, which is represented by the following expression,

$$\nu = \left(\tau - \frac{\Delta t}{2}\right)c_s^2. \tag{6}$$

When external forces act within the domain, their influence can be accounted for by including the source term S_{f_i} in the LBE, as shown in Eq. 1. There are several schemes for modeling this term in the literature. In this paper, we adopt the scheme proposed by Guo et al. [24], which is widely employed as reported by Bawazeer et al. [4]. This scheme effectively mitigates the appearance of undesired derivatives in the continuity and momentum equations resulting from time discretization artifacts, a concern present in other schemes [38]. Consequently, the source term for a given external force field $\mathbf{F}$ is expressed by Eq. 7, where $\hat{F}_i$ represents the forcing term. It is important to note that the dimensions of $\mathbf{F}$ are given in force per unit of volume (N m^{-3}).

$$S_{f_i} = \left(1 - \frac{\Delta t}{2\tau}\right)\hat{F}_i = \left(1 - \frac{\Delta t}{2\tau}\right)w_i \left[\frac{\mathbf{c_i}-\mathbf{u}}{c_s^2} + \frac{(\mathbf{c_i}\cdot\mathbf{u})\mathbf{c_i}}{c_s^4}\right]\cdot\mathbf{F} \tag{7}$$

For simulating more complex flows, the multiple-relaxation-time (MRT) collision operator, introduced by Higuera and Jiménez [29], is commonly employed within the LBE framework to enhance the method stability, particularly for low τ values [38]. Unlike the single-relaxation-time collision operator, the MRT operates in the moment space, offering improved numerical stability. Generally, the MRT can be defined as $\Omega_i^{\mathrm{MRT}} = -\left[\mathbf{M}^{-1}\mathbf{\Lambda}\mathbf{M}\right]_{ij}(f_j - f_j^{\mathrm{eq}})$, where $[\mathbf{M}]$ represents the transformation matrix and $[\mathbf{\Lambda}]$ denotes the collision matrix.

The transformation matrix is responsible for calculating the moments $\mathbf{m}$ of the distribution functions, given by $\mathbf{m} = [\mathbf{M}]\cdot\mathbf{f}$. Similarly, equilibrium moments can be obtained as $\mathbf{m}^{\mathrm{eq}} = [\mathbf{M}]\cdot\mathbf{f}^{\mathrm{eq}}$. In the dimensional LBM, particularly considering the $D2Q9$ velocity scheme, the

dimensional transformation matrix is provided by Eq. 8. In this matrix, each row corresponds to one moment of the distribution function: e represents the energy (second-order moment), ϵ the energy squared (fourth-order moment), J_x and J_y the mass fluxes (first-order moments), q_x and q_y the energy fluxes (third-order moments) and p_{xx} and p_{xy} the components of the stress tensor (second-order moments). As the matrix should be dimensional, the moments should be multiplied by the lattice speed c considering the appropriate order for each one.

$$[\mathbf{M}] = \begin{pmatrix} c^0 \cdot \mathbf{M}_\rho \\ c^2 \cdot \mathbf{M}_e \\ c^4 \cdot \mathbf{M}_\epsilon \\ c^1 \cdot \mathbf{M}_{J_x} \\ c^3 \cdot \mathbf{M}_{q_x} \\ c^1 \cdot \mathbf{M}_{J_y} \\ c^3 \cdot \mathbf{M}_{q_y} \\ c^2 \cdot \mathbf{M}_{p_{xx}} \\ c^2 \cdot \mathbf{M}_{p_{xy}} \end{pmatrix} = \begin{pmatrix} 1 & 1 & 1 & 1 & 1 & 1 & 1 & 1 & 1 \\ -4c^2 & -c^2 & -c^2 & -c^2 & -c^2 & 2c^2 & 2c^2 & 2c^2 & 2c^2 \\ 4c^4 & -2c^4 & -2c^4 & -2c^4 & -2c^4 & c^4 & c^4 & c^4 & c^4 \\ 0 & c & 0 & -c & 0 & c & -c & -c & c \\ 0 & -2c^3 & 0 & 2c^3 & 0 & c^3 & -c^3 & -c^3 & c^3 \\ 0 & 0 & c & 0 & -c & c & c & -c & -c \\ 0 & 0 & -2c^3 & 0 & 2c^3 & c^3 & c^3 & -c^3 & -c^3 \\ 0 & c^2 & -c^2 & c^2 & -c^2 & 0 & 0 & 0 & 0 \\ 0 & 0 & 0 & 0 & 0 & c^2 & -c^2 & c^2 & -c^2 \end{pmatrix} \tag{8}$$

Despite of being represented by Ω_i^{MRT}, it is common for the MRT collision step to be completely performed in the moment space. Then, the post-collision functions f_i^* are recuperated by $\mathbf{f}^* = [\mathbf{M}]^{-1} \cdot \mathbf{m}^*$, which are later used to perform the streaming process: $f_i(\mathbf{x} + \mathbf{c}_i \Delta t, t + \Delta t) = f_i^*(\mathbf{x}, t)$. For the dimensional LBM, the inverse of the transformation matrix can be given by Eq. 9, considering the $D2Q9$ velocity scheme.

$$[\mathbf{M}]^{-1} = \begin{pmatrix} \frac{1}{9} & \frac{-1}{9c^2} & \frac{1}{9c^4} & 0 & 0 & 0 & 0 & 0 & 0 \\ \frac{1}{9} & \frac{-1}{36c^2} & \frac{-1}{18c^4} & \frac{1}{6c} & \frac{-1}{6c^3} & 0 & 0 & \frac{1}{4c^2} & 0 \\ \frac{1}{9} & \frac{-1}{36c^2} & \frac{-1}{18c^4} & 0 & 0 & \frac{1}{6c} & \frac{1}{6c^3} & \frac{-1}{4c^2} & 0 \\ \frac{1}{9} & \frac{-1}{36c^2} & \frac{-1}{18c^4} & \frac{-1}{6c} & \frac{1}{6c^3} & 0 & 0 & \frac{1}{4c^2} & 0 \\ \frac{1}{9} & \frac{-1}{36c^2} & \frac{-1}{18c^4} & 0 & 0 & \frac{-1}{6c} & \frac{1}{6c^3} & \frac{-1}{4c^2} & 0 \\ \frac{1}{9} & \frac{1}{18c^2} & \frac{1}{36c^4} & \frac{1}{6c} & \frac{1}{12c^3} & \frac{1}{6c} & \frac{1}{12c^3} & 0 & \frac{1}{4c^2} \\ \frac{1}{9} & \frac{1}{18c^2} & \frac{1}{36c^4} & \frac{-1}{6c} & \frac{-1}{12c^3} & \frac{1}{6c} & \frac{1}{12c^3} & 0 & \frac{-1}{4c^2} \\ \frac{1}{9} & \frac{1}{18c^2} & \frac{1}{36c^4} & \frac{-1}{6c} & \frac{-1}{12c^3} & \frac{-1}{6c} & \frac{-1}{12c^3} & 0 & \frac{1}{4c^2} \\ \frac{1}{9} & \frac{1}{18c^2} & \frac{1}{36c^4} & \frac{1}{6c} & \frac{1}{12c^3} & \frac{-1}{6c} & \frac{-1}{12c^3} & 0 & \frac{-1}{4c^2} \end{pmatrix} \tag{9}$$

The Guo et al. [24] force scheme can be also adapted to the MRT operator [39, 40]. In this case, the collision process in the moment space is represented by Eq. 10, being $\mathbf{F_m} = [\mathbf{M}] \cdot \hat{\mathbf{F}}$ the moments of the forcing term.

$$\mathbf{m}^* = \mathbf{m} - \Delta t[\mathbf{\Lambda}] \cdot (\mathbf{m} - \mathbf{m}^{\mathrm{eq}}) + \Delta t\left([\mathbf{I}] - \frac{\Delta t}{2}[\mathbf{\Lambda}]\right) \cdot \mathbf{F_m} \tag{10}$$

The collision matrix can be defined as a diagonal matrix $[\mathbf{\Lambda}] = \text{ diag } (\omega_0, \ldots, \omega_{q-1})$, in which the main diagonal are composed by the relaxation frequencies ω_i, related to each moment of the distribution functions. In this matrix, the frequencies associated with conserved moments are zero because they are not affected by the collision process [43].

Thus, for the $D2Q9$ velocity scheme, the collision matrix is defined as $[\mathbf{\Lambda}] = \text{ diag } (0, \omega_e, \omega_\epsilon, 0, \omega_q, 0, \omega_q, \omega_\nu, \omega_\nu)$ [38]. The two last frequencies are related to the kinematic viscosity of the fluid, being defined as $\omega_\nu = 1/\tau$. Also, the relaxation frequency related to the energy can be associated with the bulk viscosity of the fluid as $\eta = (\omega_e^{-1} - 0.5\Delta t)c_s^2$ [23]. The other frequencies can be chosen without significant effects in the transport coefficients, and values between $1/\Delta t$ and $2/\Delta t$ are recommended. The third-order relaxation parameter for the dimensional LBM is redefined as $\omega_q = (3/\Delta t)(2/\Delta t - \omega_\nu)/(3/\Delta t - \omega_\nu)$. This relation was initially obtained by Lallemand and Luo [43], and here, we made the necessary changes to guarantee corresponding third-order relaxation parameter for the dimensional LBM, as now the relaxation frequencies (ω) have units of $[1/s]$. We can obtain the macroscopic quantities of interest taking the zero and first moments of the distribution function f_i [75]. Considering the force scheme, these moments are calculated by Eqs. 11 and 12, respectively, for both BGK and MRT collision operators.

$$\rho(\mathbf{x}, t) = \sum_{i=0}^{q-1} f_i(\mathbf{x}, t) \tag{11}$$

$$\mathbf{u}(\mathbf{x}, t)\rho(\mathbf{x}, t) = \sum_{i=0}^{q-1} \mathbf{c_i} f_i(\mathbf{x}, t) + \frac{\Delta t}{2}\mathbf{F}(\mathbf{x}, t) \tag{12}$$

In the simulations conducted in this paper, we employed the *link-wise* scheme for formulating the boundary conditions. In this scheme, the boundaries are positioned on lattice links, situated at a distance of $0.5\Delta x$ from the physical boundaries of the domain [38].

In the simulations of fluid flow, we utilized five primary boundary conditions (BC): inlet with prescribed velocity, outlet at atmosphere pressure, periodic boundaries, fixed non-slip walls, and symmetric boundaries. For both inlet and fixed walls, we considered the bounce-back scheme [41, 42], represented by Eq. 13.

In this equation, $\bar{i}$ denotes the opposite direction of i, $\mathbf{u_w}$ and ρ_w represent the boundary velocity and density, respectively, and $\mathbf{x_b}$ is the position of the boundary node. For fixed walls, the BC simplifies to $f_{\bar{i}}(\mathbf{x_b}, t+\Delta t) = f_i^*(\mathbf{x_b}, t)$.

For the fluid outlet, we used the anti-bounce-back scheme [22], which is expressed by Eq. 14.

$$f_{\bar{i}}(\mathbf{x_b}, t+\Delta t) = f_i^*(\mathbf{x_b}, t) - 2w_i\rho_w \frac{\mathbf{c_i}\cdot\mathbf{u_w}}{c_s^2} \tag{13}$$

To maintain atmosphere pressure using this BC, we set ρ_w equal to the fluid density at atmospheric pressure. Usually, this is the average density of the fluid in an equilibrium state. Additionally, the velocity is calculated by extrapolation: $\mathbf{u_w} \approx \mathbf{u}(\mathbf{x_b}, t) + 0.5[\mathbf{u}(\mathbf{x_b}, t) - \mathbf{u}(\mathbf{x_{b-1}}, t)]$. Here, $\mathbf{x_{b-1}}$ represents the next node inside the domain in the normal direction of the boundary [38].

$$f_{\bar{i}}(\mathbf{x_b}, t+\Delta t) = -f_i^*(\mathbf{x_b}, t) + 2w_i\rho_w \left[1 + \frac{(\mathbf{c_i}\cdot\mathbf{u_w})^2}{2c_s^4} - \frac{\mathbf{u_w}\cdot\mathbf{u_w}}{2c_s^2}\right] \tag{14}$$

The symmetric boundaries are implemented using Eq. 15 [38]. In this equation, j represents the indices of the population with same tangential velocity as i but with opposite normal velocity, defined as $(c_{j,\tan}; c_{j,n}) = (c_{i,\tan}; -c_{i,n})$.

For instance, if we consider the top boundary as symmetric, and for the $D2Q9$ velocity scheme, there are three unknown distribution functions: f_4, f_7 and f_8. As a result, f_6 has the same tangential velocity as f_7 (where $\mathbf{c_6} = c(-1, 1)$ and $\mathbf{c_7} = c(-1, -1)$), but opposite normal velocity. Therefore $f_7(\mathbf{x_b} + \mathbf{c_{7,tan}}\Delta t, t+\Delta t) = f_6^*(\mathbf{x_b}, t)$. Considering the tangential velocity of f_7 as $c_{7,\tan} = -c$, the final relation becomes $f_7(\mathbf{x_b} - (\Delta x, 0), t+\Delta t) = f_6^*(\mathbf{x_b}, t)$. The same procedure can be applied to the other functions.

$$f_j(\mathbf{x_b} + \mathbf{c_{j,tan}}\Delta t, t+\Delta t) = f_i^*(\mathbf{x_b}, t) \tag{15}$$

Lastly, for the periodic boundaries, the leaving distribution functions at one side are the unknown functions that arrive at the opposite boundary. Then, this BC can be represented by $f_i(\mathbf{x_b}, t+\Delta t) = f_i^*(\mathbf{x_b} + \mathbf{L} - \mathbf{c_i}\Delta t, t)$, being $\mathbf{L}$ the size of the domain at the normal direction of the boundary.

2.2 Dimensional thermal LBM

Because of its generality, the LBM can be also used to simulate heat transfer problems. There are several methods proposed in the literature to deal with heat transfer [23]. In this case, we chose the double-distribution-function model.

In this model, it is defined another distribution function g_i for the temperature field T [23, 32]. Thus, while the *momentum* evolution is simulated by Eq. 2, the evolution of the temperature field is calculated by Eq. 16 for the BGK operator [11].

$$g_i(\mathbf{x} + \mathbf{c_i}\Delta t, t+\Delta t) - g_i(\mathbf{x}, t) = -\frac{\Delta t}{\tau_T}\left[g_i(\mathbf{x}, t) - g_i^{\mathrm{eq}}(\mathbf{x}, t)\right] + S_{g_i}(\mathbf{x}, t)\Delta t \tag{16}$$

By the Chapman–Enskog analysis, we can recover the energy conservation equation, given a relation between the relaxation time of the thermal LBE, τ_T, and the thermal diffusivity of the fluid α: $\alpha = (\tau_T - 0.5\Delta t)c_s^2$. This relation represents the link between the LBE and the energy equation.

In this case, the source term is related to the volumetric heat source instead of external forces and can be similarly formulated by Eq. 17 [27, 38]. It is important to note that $\dot{q}$ has units of [K s^{-1}], because it is defined as $\dot{q} = q'''/(\rho c_p)$, were q''' is the volumetric heat source in (W m^{-3}) and c_p stands for the specific heat at constant pressure of the material in (J kg^{-1}K^{-1}).

$$S_{g_i} = \left(1 - \frac{\Delta t}{2\tau}\right) w_i \dot{q} \tag{17}$$

The equilibrium distribution function, g_i^{eq}, considered in Eq. 16, is related to the temperature and can be defined by Eq. 18.

$$g_i^{\mathrm{eq}}(\mathbf{x}, t) = w_i T(\mathbf{x}, t)\left(1 + \frac{\mathbf{c_i}\cdot\mathbf{u}}{c_s^2}\right)_{(\mathbf{x},t)} \tag{18}$$

It should be mention that in the previous relation, we used a linear velocity-dependent form of the equilibrium distribution function [38]. But if necessary, it is also possible to consider a second-order formulation, given by: $g_i^{\mathrm{eq}} = w_i T\left[1 + \frac{\mathbf{c_i}\cdot\mathbf{u}}{c_s^2} + \frac{(\mathbf{c_i}\cdot\mathbf{u})^2}{2c_s^4} - \frac{\mathbf{u}\cdot\mathbf{u}}{2c_s^2}\right]$. For the simulations performed in this work, we used only the first-order equilibrium distribution function (Eq. 18), being enough for the desired results.

The macroscopic temperature can be found from the zero moment of the distribution function g_i. However, differently than for the flow simulation, in the presence of volumetric heat generation, it is necessary to add an extra term to this moment of g_i, as shown in Eq. 19 [69].

$$T(\mathbf{x}, t) = \sum_{i=0}^{q-1} g_i(\mathbf{x}, t) + \frac{\Delta t}{2}\dot{q}(\mathbf{x}, t) \tag{19}$$

We also used the MRT collision operator for the thermal LBM. In this case, considering the $D2Q9$ velocity set, the collision matrix can assume again the diagonal form. In this paper, it will be used the same relaxation parameter as employed in Martins and Gómez [55], but adapted for the dimensional LBM

$[\mathbf{\Lambda}_T] = \text{diag}\,(0, 1/\Delta t, 1/\Delta t, \omega_T, 1/\Delta t, \omega_T, 1/\Delta t, 1/\Delta t, 1/\Delta t)$, being $\omega_T = 1/\tau_T$. The transformation matrices remain equal to those used for the simulation of fluid flow.

For the heat transfer simulations with the thermal LBM, five kinds of boundary conditions were considered: inlet with prescribed temperature, fixed walls with prescribed heat flux, fixed walls with prescribed temperature, outlet and symmetric boundaries.

For inlets with fixed temperature, we used the anti-Bounce-Back scheme [19, 45, 86]. This BC is given by Eq. 20, where g_i^* is the post-collision distribution function, $\bar{i}$ is the opposite direction to i, $\mathbf{x_b}$ represents the coordinates of the boundary node and the subscript w indicates the variables values at the boundary wall.

$$g_{\bar{i}}(\mathbf{x_b}, t + \Delta t) = -g_i^*(\mathbf{x_b}, t) + 2w_i T_w \left[1 + \frac{(\mathbf{c_i} \cdot \mathbf{u_w})^2}{2c_s^4} - \frac{\mathbf{u_w} \cdot \mathbf{u_w}}{2c_s^2}\right] \tag{20}$$

The same BC can be also used to treat fixed walls with prescribed temperatures [38]. In this case, the boundary velocity $\mathbf{u_w}$ is set to zero and the BC reduces itself to $g_{\bar{i}}(\mathbf{x_b}, t + \Delta t) = -g_i^*(\mathbf{x_b}, t) + 2w_i T_w$.

The fixed wall Neumann BC (prescribed heat flux) was modeled with the scheme given by Li et al. [46], considering the $D2Q9$ velocity set with the halfway boundary. This scheme is based on the modification of proposed by Yoshida and Nagaoka [84] for the $D2Q5$. This BC is given by Eq. 21, where λ_i is a constant and q'' is the heat flux normal to the boundary (units of [W m^{-2}]). There are many possible values of λ_i according to Li et al. [46], but we propose the adoption of $\lambda_i = 2w_i/c_s^2$, giving $\lambda_{1,2,3,4} = 4/6$ and $\lambda_{5,6,7,8} = 1/6$.

$$g_{\bar{i}}(\mathbf{x_b}, t + \Delta t) = g_i^*(\mathbf{x_b}, t) + \lambda_i \left(\frac{\Delta t}{\Delta x}\right)\left(\frac{q''}{\rho c_p}\right) \tag{21}$$

The symmetry boundary condition is the same used for the fluid moment distribution functions, as previously explained in Sect. 2.1.

For the outlets, we considered the first-order extrapolation scheme: $g_i(\mathbf{x_b}, t + \Delta t) = g_i(\mathbf{x_{b-1}}, t + \Delta t)$. It is important to mention that the first-order scheme was used instead of the second-order one because the first is more stable than the second [59].

2.3 Dimensional LBM version for two-phase systems

There are several LBM models in the literature tailored for multiphase and multicomponent systems [23, 30, 47, 66, 71, 72, 76]. In this paper, we provide a brief overview of the model proposed by Liang et al. [52], and subsequently, we adapt it for simulating two-phase systems using the new proposed dimensional approach. This multiphase model is founded on the evolution of two distribution functions: h_i and z_i, designed to capture the movement of the interface and the pressure field, respectively.

These authors have developed a model akin to those proposed by Ren et al. [64] and Wang et al. [78], which relies on utilizing the conservative Allen–Cahn equation for interface tracking. The Allen–Cahn equation, depicted in Eq. 22, serves as the cornerstone of their approach [13]. In this equation, ϕ denotes the order parameter, responsible for delineating the regions occupied by each phase, where $\phi = 1$ corresponds to the liquid phase and $\phi = 0$ represents the gas phase. Additionally, W symbolizes the interface width, as the model considers a diffuse interface between the distinct phases, while M represents the mobility and $\mathbf{n}$, the normal direction to the interface, calculable as $\mathbf{n} = \nabla\phi/|\nabla\phi|$.

$$\partial_t \phi + \nabla \cdot (\phi \mathbf{u}) = \nabla \cdot \left[M\left(\nabla\phi - \frac{4\phi(1-\phi)}{W}\mathbf{n}\right)\right] \tag{22}$$

Considering the BGK collision operator, the LBE responsible for the interface tracking, linked to h_i functions, is represented by Eq. 23. The source term S_{h_i} is formulated to ensure the recovery of Eq. 22 through the Chapman–Enskog analysis. Consequently, this term is expressed by Eq. 24.

$$h_i(\mathbf{x} + \mathbf{c_i}\Delta t, t + \Delta t) - h_i(\mathbf{x}, t) = -\frac{\Delta t}{\tau_\phi}\left[h_i(\mathbf{x}, t) - h_i^{\text{eq}}(\mathbf{x}, t)\right] + S_{h_i}(\mathbf{x}, t)\Delta t \tag{23}$$

$$S_{h_i} = \left(1 - \frac{\Delta t}{2\tau_\phi}\right) w_i \frac{\mathbf{c_i} \cdot \left[\partial_t(\phi\mathbf{u}) + c_s^2 \frac{4\phi(1-\phi)}{W}\mathbf{n}\right]}{c_s^2} \tag{24}$$

The temporal derivative in Eq. 24 can be computed using the explicit Euler scheme: $\partial_t(\phi\mathbf{u}) \approx [\phi(t)\mathbf{u}(t) - \phi(t - \Delta t)\mathbf{u}(t - \Delta t)]/\Delta t$ [53]. Furthermore, τ_ϕ represents the relaxation time for the interface tracking LBE, associated with the mobility value as $M = (\tau_\phi - 0.5\Delta t)c_s^2$. The equilibrium distribution function is calculated considering a first-order expansion, as shown in Eq. 25.

$$h_i^{\text{eq}}(\mathbf{x}, t) = w_i \phi(\mathbf{x}, t)\left(1 + \frac{\mathbf{c}_i \cdot \mathbf{u}}{c_s^2}\right)_{(\mathbf{x},t)} \tag{25}$$

Similarly to the traditional LBM, we can obtain the macroscopic quantities by the moments of the distribution functions. Thus, the order parameter is calculated by the zero moment of h_i using Eq. 26, and both the macroscopic density and kinematic viscosity are calculated as a linear function of ϕ, such as $\rho = \rho_g + \phi(\rho_l - \rho_g)$ and $\nu = \nu_g + \phi(\nu_l - \nu_g)$.

In these relations, the subscripts g and l refer to the gas and liquid properties, respectively.

$$\phi(\mathbf{x},t)=\sum_{i=0}^{q-1}h_i(\mathbf{x},t) \tag{26}$$

In the case of pressure evolution, the original authors employed an incompressible transformation similar to that proposed by He et al. [28], resulting in Eq. 27 for the BGK collision operator. Importantly, it should be noted that the MRT operator can also be used to perform the collision process for z_i functions, applying Eq. 10 for the moments of these functions. For the $D2Q9$ model, the adopted values for the collision matrix are $[\mathbf{\Lambda}]=\text{diag}\,(1/\Delta t,1/\Delta t,1/\Delta t,1/\Delta t,\omega_{q2},1/\Delta t,1/\Delta t,1/\tau,1/\tau)$, with $\omega_{q2}=(3/\Delta t)(2/\Delta t-\omega_\nu)/(3/\Delta t-\omega_\nu)$.

$$\begin{aligned}&z_i(\mathbf{x}+\mathbf{c_i}\Delta t,t+\Delta t)-z_i(\mathbf{x},t)\\&\quad=-\frac{\Delta t}{\tau}\left[z_i(\mathbf{x},t)-z_i^{\text{eq}}(\mathbf{x},t)\right]+S_{z_i}(\mathbf{x},t)\Delta t\end{aligned} \tag{27}$$

For calculating the equilibrium distribution functions, the authors proposed Eq. 28 to satisfy the divergence-free condition. In this equation, s_i represents the term computed using Eq. 29 [49, 50]. Additionally, in Eq. 28, p is defined as the total pressure.

$$z_i^{\text{eq}}(\mathbf{x},t)=\begin{cases}\frac{p(\mathbf{x},t)}{c_s^2}(w_i-1)+\rho(\mathbf{x},t)s_i(\mathbf{u}),\ \text{if } i=0\\ \frac{p(\mathbf{x},t)}{c_s^2}w_i+\rho(\mathbf{x},t)s_i(\mathbf{u}),\ \text{if } i\neq 0\end{cases} \tag{28}$$

$$s_i(\mathbf{u})=w_i\left(\frac{\mathbf{c}_i\cdot\mathbf{u}}{c_s^2}+\frac{(\mathbf{c}_i\cdot\mathbf{u})^2}{2c_s^4}-\frac{\mathbf{u}\cdot\mathbf{u}}{2c_s^2}\right)_{(\mathbf{x},t)} \tag{29}$$

To recover the NSE for a two-phase system, as represented by Eq. 30 (where ζ is the dynamic viscosity), the relaxation time is once again related to the kinematic viscosity as $\nu=(\tau-0.5\Delta t)c_s^2$. In this scenario, two types of body forces are employed. $\mathbf{F_b}$ is defined as the body force acting over the domain, while $\mathbf{F_s}$ represents the force related to surface tension at the interface. Various methods exist in the literature for calculating this force, but in this paper, we considered the potential form, which is related to the chemical potential (μ) as: $\mathbf{F_s}=\mu\nabla\phi$ [33, 88]. Therefore, the forcing term for the pressure evolution LBE is defined by Eq. 31 [53].

$$\begin{aligned}&\frac{\partial(\rho\mathbf{u})}{\partial t}+\nabla\cdot(\rho\mathbf{u}\mathbf{u})\\&\quad=-\nabla p+\nabla\cdot[\zeta(\nabla\mathbf{u}+\nabla\mathbf{u}^T)]+\mathbf{F_s}+\mathbf{F_b}\end{aligned} \tag{30}$$

$$\begin{aligned}S_{z_i}&=\left(1-\frac{\Delta t}{2\tau}\right)\hat{F}_i^z\\&=\left(1-\frac{\Delta t}{2\tau}\right)w_i\left[\frac{\mathbf{c_i}\cdot(\mathbf{F_s}+\mathbf{F_b})}{c_s^2}+\frac{(\mathbf{u}\nabla\rho):(\mathbf{c_i}\mathbf{c_i})}{c_s^2}\right]\end{aligned} \tag{31}$$

Now, the macroscopic quantities related to the pressure and momentum of the fluid are described by Eqs. 32 and 33, respectively. It is noteworthy that in these equations, the pressure depends on the velocity. Therefore, it must be calculated after obtaining the velocity from Eq. 33.

$$\begin{aligned}p(\mathbf{x},t)=&\frac{c_s^2}{(1-w_0)}\\&\left[\sum_{i=1}^{q-1}z_i(\mathbf{x},t)+\frac{\Delta t}{2}\mathbf{u}(\mathbf{x},t)\cdot\nabla\rho(\mathbf{x},t)+\rho(\mathbf{x},t)s_0(\mathbf{u})\right]\end{aligned} \tag{32}$$

$$\mathbf{u}(\mathbf{x},t)\rho(\mathbf{x},t)=\sum_{i=0}^{q-1}\mathbf{c_i}z_i(\mathbf{x},t)+\frac{\Delta t}{2}\left[\mathbf{F_s}(\mathbf{x},t)+\mathbf{F_b}(\mathbf{x},t)\right] \tag{33}$$

The knowledge of the chemical potential, μ, is crucial for conducting simulations using the presented LBM. This thermodynamic property can be derived from the free energy, Ψ, of the two-phase system [63]. The free energy is a function of density and given the linear relation between ρ and ϕ, the chemical potential can be determined as: $\mu=\partial_\phi\Psi(\phi)$. The total free energy of the system is computed using Eq. 34, where $\psi(\phi)$ denotes the volumetric free energy (or the potential), and κ is a constant associated to the strength of the surface tension [34].

$$\Psi=\int_V\psi(\phi)+\frac{\kappa}{2}|\nabla\phi|^2\text{d}V \tag{34}$$

In regions close to the critical point, certain simplifications of the fluid equation of state (EoS) can be applied [67]. One widely used simplification is expressed as follows: $\psi(\phi)\approx\beta\phi^2(1-\phi)^2$, where β represents a constant. Although originally developed for regions near the critical point, this approximation has found widespread application in multiphase LBM models based on mean-field theory [16, 17, 44, 87].

Given that $\mu=\partial_\phi\Psi(\phi)=\partial_\phi\psi-\kappa\nabla^2\phi$ [7], the chemical potential can be determined using Eq. 35. Here, the constants κ and β are intricately linked to both the interface thickness (W) and the surface tension of the fluid (σ) through relationships $\kappa=\frac{3}{2}\sigma W$ and $\beta=\frac{12\sigma}{W}$.

$$\mu=\partial_\phi\psi-\kappa\nabla^2\phi=4\beta\phi(\phi-1)(\phi-0.5)-\kappa\nabla^2\phi \tag{35}$$

Furthermore, the equilibrium of a planar interface between two phases can be effectively represented by Eq. 36, where $\gamma(\mathbf{x})$ denotes the coordinate perpendicular to the interface. To prevent instabilities, we initialize both the macroscopic

density and ϕ with this equilibrium profile at the onset of the simulations.

$$\phi(\mathbf{x}) = \frac{1}{2} + \frac{1}{2}\tanh\left(\frac{2\gamma(\mathbf{x})}{W}\right) \tag{36}$$

In previous equations, such as Eq. 35, it becomes evident that computing the second-order derivative of ϕ is necessary. Utilizing the linear relationship between ρ and ϕ, we can express density gradients as $\nabla\rho = (\rho_l - \rho_g)\nabla\phi$. Thus, density gradient calculations can be performed via the first derivative of ϕ. Following the approach outlined by Liang et al. [52], spatial gradients and the Laplacian of ϕ can be efficiently computed using a second-order isotropic central scheme, as described by Eqs. 37 and 38, respectively.

$$\nabla\phi(\mathbf{x}) = \sum_{i\neq 0} \frac{w_i \mathbf{c_i}\phi(\mathbf{x} + \mathbf{c_i}\Delta t)}{c_s^2 \Delta t} \tag{37}$$

$$\nabla^2\phi(\mathbf{x}) = \sum_{i\neq 0} \frac{2w_i\left[\phi(\mathbf{x} + \mathbf{c_i}\Delta t) - \phi(\mathbf{x})\right]}{c_s^2 \Delta t^2} \tag{38}$$

In relation to the interface normal vector, it is important to mention that its calculation in the numerical code must be performed carefully. This vector is defined as $\mathbf{n} = \nabla\phi/|\nabla\phi|$, and thus, there are nodes were $|\nabla\phi| = 0$. Consequently, the division by this term can result in extremely high values. Therefore, the division is performed only where $|\nabla\phi| \neq 0$, otherwise $\mathbf{n} = \mathbf{0}$.

2.4 Limitations of dimensional LBM

It should be noted that the limitations of the dimensional LBM are the same as for the traditional LBM, as the main equations of the method, namely the LBE and BC, are essentially the same. The only difference is that in the dimensional LBM, the non-dimensionalization process is ignored, and all the variables are treated directly in their respective physical (SI) units. These limitations are manly related to the choice of the relaxation parameter τ and a limit for the maximum value of cell velocity.

For instance, considering the BGK collision operator for the $D2Q9$ scheme and the traditional equilibrium distribution function f_i^{eq} for fluid flow (Eq. 3), τ must not be too close to $\Delta t/2$ (or $\tau > \Delta t/2$), and the maximum velocity in any cell must satisfy $|\mathbf{u_{max}}| < \sqrt{1/3}\Delta x/\Delta t$ [38]. This condition applies to both dimensional and traditional LBM. However, for the traditional LBM, as the non-dimensional process is performed, these conditions becomes $\tilde{\tau} > 1/2$ and $|\tilde{\mathbf{u}}_{\max}| < \sqrt{1/3}$, because generally $\Delta\tilde{x} = \Delta\tilde{t} = 1$ l.u. (the $\tilde{}$ indicates variables in lattice units, also represented as l.u.).

It is also important to emphasize that the requirements of low-density variations and low Mach numbers, which must be satisfied by the traditional LBM for the simulation of incompressible flows, are also met by the dimensional LBM.

2.5 Application of dimensional LBM for non-dimensional problems

The non-dimensionalization process utilized in traditional CFD methods proves beneficial when the problem can be characterized with a known set of non-dimensional parameters, such as Reynolds, Rayleigh or Weber numbers, for example. This approach is advantageous because it allows multiple problems to be reduced to the same non-dimensional problem through similarity. Typically, in such cases, the macroscopic equations like the Navier–Stokes equation (NSE) or energy conservation equation are non-dimensionalized, and the problem is numerically solved using non-dimensional variables.

First and foremost, it is crucial to differentiate between the non-dimensionalization process just described and the one conducted in traditional lattice Boltzmann method (LBM). While the former aims to generalize the mathematical formulation of the problem, attempting to represent the phenomenon through a set of non-dimensional parameters, the latter involves transforming from physical space to lattice space, where $\Delta\tilde{t} = \Delta\tilde{x} = 1$ l.u. This transformation is not necessarily solely based on the non-dimensional numbers characterizing the problem.

Hence, the dimensional LBM can be employed to solve the non-dimensional form of physical problems, meaning the solution of non-dimensional macroscopic equations using the dimensional LBE (without transitioning to lattice space). Consequently, the only modifications entail the relationship between relaxation parameters and macroscopic equations, along with the utilization of entirely dimensionless variables.

For instance, let's consider an isothermal incompressible lid-driven cavity flow, where the governing equations are represented by the NSE. If we neglect the influences of gravity and wall roughness, the Reynolds number emerges as the key non-dimensional parameter characterizing the flow dynamics, given by $\text{Re} = \rho U_w L/\zeta$, where L represents a characteristic length (such as the channel height), ρ denotes the fluid density, ζ stands for the fluid dynamic viscosity and U_w signifies the lid velocity. Subsequently, by denoting the non-dimensional variables with asterisks $*$, the non-dimensionalized form of the NSE can be expressed as follows:

$$\frac{D^*\mathbf{u}^*}{Dt^*} = -\nabla^* p^* + \frac{1}{\text{Re}}\nabla^{*2}\mathbf{u}^*. \tag{39}$$

Thus, with the BGK collision operator, through the Chapman–Enskog analysis, the relaxation time becomes linked to the Reynolds number rather than the kinematic viscosity: $\text{Re}^{-1} = (\tau^* - 0.5\Delta t^*)c_s^{*2}$. Consequently, we can proceed to

solve the problem using the dimensional LBM. However, in this approach, we must non-dimensionalize the macroscopic fields (velocity, pressure and density) by ρ, V and L and the previous relation for the relaxation parameter.

The distinction lies in the fact that the variables denoted by $*$ arise from the traditional non-dimensionalization process, aiming to generalize the problem through a set of non-dimensional parameters, while those represented by $\tilde{}$ originate from the transformation to the lattice space, characteristic of conventional LBM's non-dimensionalization approach.

We observe that the conversion to the lattice space is not a prerequisite for solving non-dimensional problems. The dimensional LBM presented here enables the solution of such problems directly, essentially entailing the solution of the non-dimensionalized macroscopic equations without conversion to lattice units.

For the sake of comparison, we solved an example in Sect. 3.2 with the dimensional LBM considering the NSE both in physical units and in its non-dimensional form, and also with the traditional LBM. We compared the results between them and performed a stability analysis of the three approaches.

3 Results

In this section, we present the simulation results obtained with the proposed dimensional LBM for five main problems. The results are compared with those of conventional LBM to verify that both methods achieve the same results. Furthermore, to evaluate the performance and accuracy of the LBM, the numerical results were compared with a reference solution, being analytical when available, from finite difference (FD) solutions or from literature. For these comparisons, we use the relative error norm L_2 [20, 65], here called "global error" and defined by Eq. 40.

For the case in which the FD solution was taken as a reference, we carried out a convergence study to ensure the good quality of these reference results. To achieve this objective, it was established that the global errors between two consecutive simulations, one with a grid size of Δx and the other with $\Delta x_{\text{next}} = \Delta x/2$ (reference solution), must be less than or equal to 0.01%, meaning $E_2 \leq 0.01\%$.

$$E_2(\%) = 100\sqrt{\frac{\sum_{\mathbf{x}}(\chi_{\text{ref}} - \chi_{\text{num}})^2}{\sum_{\mathbf{x}} \chi_{\text{ref}}^2}} \tag{40}$$

As LBM is naturally a transient numerical method, to check whether the numerical solutions have reached the steady state, we apply the condition given by Eq. 41. In this relationship, χ represents the main variable to be verified (velocity for Poiseuille flow or temperature for forced convection problems, for example), and $\tilde{t} + 1000$ is the instant of 1000 steps of time after $\tilde{t}$.

$$\max\left[\chi(\mathbf{x}, \tilde{t} + 1000) - \chi(\mathbf{x}, \tilde{t})\right] \leq 10^{-8} \tag{41}$$

Furthermore, three stability analyzes were performed comparing the stable regions in the graph Δt:Δx for both conventional and dimensional LBM. We selected one benchmark problem for each LBM model: the lid-driven cavity for fluid flow LBM (Sect. 2.1); forced convection in a hydrodynamic channel developed for thermal LBM (Sect. 2.2); and the static bubble test for the multiphase LBM model (Sect. 2.3).

In simulations, the procedure for choosing the values Δx and Δt for the dimensional LBM is similar to that of other explicit numerical methods (finite difference or finite volume methods, for example). First we define arbitrary values of Δx and Δt, which must always respect the stability conditions (see Sect. 2). Next, we perform a spatial analysis of the grid size to check the convergence of the solution, stopping when the desired convergence is reached. In this analysis, Δt can be left unchanged or changed if necessary to achieve stability. For more complex cases, the stability of the simulations can be improved using the MRT collision operator. As the non-dimensionalization process is not performed for the dimensional LBM, the adjustment of Δx and Δt can be performed directly and simply, in a similar way to the traditional numerical methods mentioned previously.

All thermodynamic and transport properties employed for the fluid simulations were calculated using the free Coolprop python library [5].

3.1 One-dimensional heat diffusion

The first problem relates to determine the axial temperature distribution of a fuse used to prevent a power electronic module from breaking due to a high current. This problem was taken from Nellis and Klein [61], problem 3.8–1, and we address it here because it presents an interesting engineering problem involving one-dimensional heat conduction.

The fuse is a wire (without insulation) with length $L = 0.08$ m and diameter $d = 0.0015$ m. Heat is lost from the surface of the fuse through convection to the surrounding air at $T_\infty = 20\,^\circ$C with a heat transfer coefficient of $\overline{h} = 5$ W m^{-2} K^{-1}. The fuse is made of an aluminum alloy with the following properties, assumed constant: $\rho = 2700$ kg m^{-3}, $k = 150$ W m^{-1}K^{-1}, $c_p = 900$ J kg^{-1}K^{-1} and electrical resistivity of res $= 1 \cdot 10^{-7}\,\Omega$ m.

Initially, the fuse has an uniform temperature of $T_{\text{ini}} = T_\infty = 20\,^\circ$C. At this point, it is subjected to a current of $I_e = 100A$, resulting in uniform volumetric heat generation within the fuse material. Both ends of the fuse ($x = 0$ and

$x = L$) are maintained at a constant temperature of $T_w = 20\,°\text{C}$. The objective is to determine the axial temperature variation of the fuse, neglecting radial and angular temperature variations due to the small diameter of the fuse.

The governing equation for the energy conservation in the fuse is represented by Eq. 42. This equation is derived considering that the heat generated due to the current passing through the fuse is modeled as $q''' = (16I_c^2\text{res})/(\pi^2 d^4)$, and that the total heat lost by convection per unit of volume is given by $\dot{Q}'''_{\text{conv}} = (\pi dL)\bar{h}(T - T_\infty)/(0.25\pi d^2 L) = 4\bar{h}(T - T_\infty)/d$.

$$\frac{\partial T}{\partial t} = \alpha \frac{\partial^2 T}{\partial x^2} + \frac{q'''}{\rho c_p} - \frac{4\bar{h}(T - T_\infty)}{\rho c_p d} \tag{42}$$

We examined both transient and steady-state solutions of the problem, employing both LBM models with BGK collision operator using the $D1Q3$ velocity scheme. The corresponding lattice velocities are $\mathbf{c_0} = 0$, $\mathbf{c_1} = c$ and $\mathbf{c_2} = -c$, with the respective weights, $w_0 = 4/6$, $w_1 = 1/6$ and $w_2 = 1/6$. The sound speed remains $c_s = c/\sqrt{3}$ [62]. In all simulations, we employed the discrete time and space intervals of $\Delta x = 4 \cdot 10^{-4}$ m and $\Delta t = 2.5 \cdot 10^{-4}$ s. We calculated a single source term for the LBM considering the sum of volumetric heat generation and convective losses as $\dot{q} = q'''/(\rho c_p) - 4\bar{h}(T - T_\infty)/(\rho c_p d)$. To avoid implicitness with the LBM, the convective losses were calculated using the temperature determined from the previous time step. Regarding the BCs, we implemented fixed temperatures at $x = 0$ and $x = L$ using Eq. 20.

The transient LBM results were compared with numerical solutions obtained using the FD method. We employed a forward time central space scheme to solve Eq. 42, with $\Delta x_{\text{FDM}} = 4.0 \cdot 10^{-4}$ m and $\Delta t_{\text{FDM}} = 2.5 \cdot 10^{-4}$ s, ensuring that $E_2 \leq 0.01\%$. The steady-state LBM results were compared against the analytical solution provided by Eq. 43, where $m = \sqrt{(\bar{h}\text{Per})/(kA_c)}$, and Per and A_c are the fuse perimeter and cross-sectional area, respectively.

$$T(x) = \left(T_w - T_\infty - \frac{\dot{q}'''A_c}{\bar{h}\text{Per}}\right) \cdot \left[\left(1 + \frac{e^{mL} - 1}{e^{-mx} - e^{mx}}\right)e^{mx} + \left(\frac{1 - e^{mL}}{e^{-mx} - e^{mx}}\right)e^{-mx}\right] + T_\infty + \frac{\dot{q}'''A_c}{\bar{h}\text{Per}} \tag{43}$$

The transient solutions for conventional and dimensional LBM, as well as for the FD method at various times, along with the global errors between each LBM and FD solutions, are presented in Figs. 2a, b, respectively. The transient solutions exhibit the expected physical behavior, demonstrating an increase in fuse temperature over time, with the highest temperatures observed at the middle lengths of the fuse. The relative errors diminish with time as the system approaches a steady-state regime, and they remain small for all cases. Both LBM models yield identical results.

The steady-state solutions obtained with LBM models and the analytical solution given by Eq. 43 are depicted in Fig. 3. The stationary results accurately portray the temperature distribution, with the maximum temperature occurring at the middle of fuse length. It is worth noting that we only present this temperature distribution for the purpose of comparison between the LBM and analytical solutions, as the fuse alloy would melt at approximately 500 °C. The global relative errors for the stationary

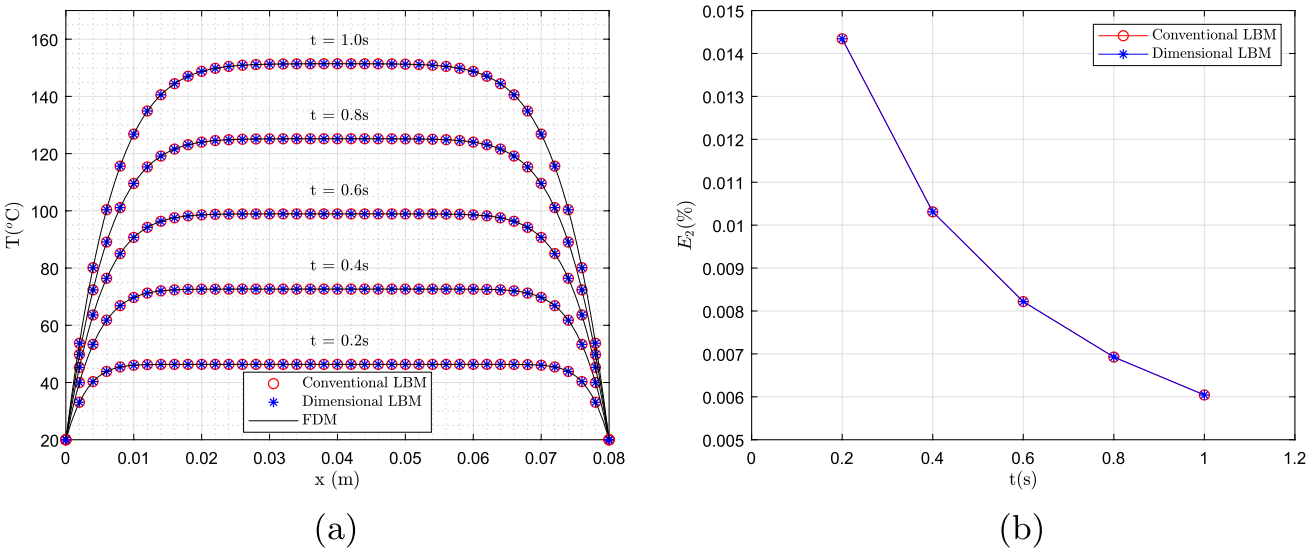

Fig. 2 **a** One-dimensional axial temperature variation of the fuse for some time steps, obtained by the FD scheme and the conventional and dimensional LBM. **b** Temporal variation of the global errors for the conventional and dimensional LBM, in comparison with the FD solutions

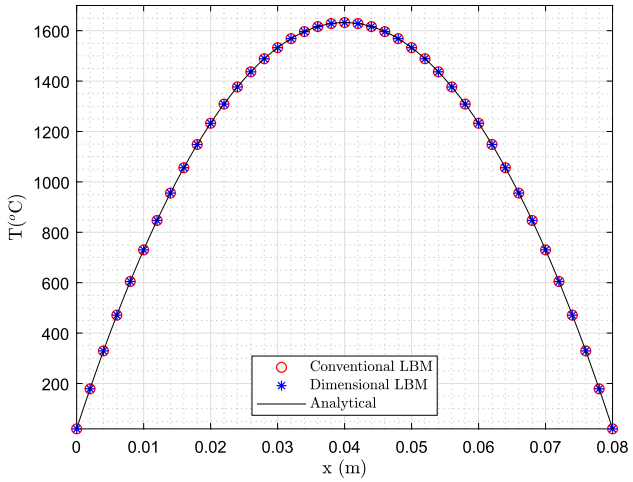

Fig. 3 Steady-state axial fuse temperature distribution for the numerical and analytical solutions

solution were consistent for the conventional and the dimensional LBM, with $E_2^{\text{dim}} = E_2^{\text{conv}} = 0.0029\%$.

In this example, we observed that both the dimensional and the conventional LBM yielded identical results with very good accuracy compared the reference solutions. This finding indicates that the proposed dimensional LBM can be confidently used, and that the non-dimensionalization process can be avoided without affecting the results obtained with the method.

3.2 Lid-driven cavity

After solving a pure heat diffusion problem, we proceeded to address a 2D isothermal and incompressible fluid flow problem: the lid-driven flow in a square cavity. We considered water at 25°C and 1 atm as the working fluid, with properties summarized in Table 2 (liquid properties in first column). The square cavity has dimension $L = 2.5$ mm. To ensure comparability with benchmark solutions from literature [21], the Reynolds number was set to $\text{Re} = 1000$. The Reynolds number is defined as $\text{Re} = U_w L/\nu$, allowing us to determine the lid speed from this non-dimensional parameter.

Here, we considered the steady-state solution obtained with a 250×250 grid using both the traditional and the dimensional LBM. Additionally, with the dimensional LBM, we solved both the physical and non-dimensional NSE, as explained in Sect. 2.5. The BGK collision operator was employed for all the three approaches.

The results for the dimensional LBM are depicted in Fig. 4, while the comparison against the literature solution is presented in Fig. 5. As expected, the three LBM approaches (dimensional LBM, dimensional LBM with non-dimensional NSE and conventional LBM) exhibited the same global deviation in relation to the reference numerical solution: 1.9513%. This deviation was calculated by Eq. 40.

Next, we investigated how the value of $|\mathbf{u}|^{\max}$ that guarantees stability changes with the $\Delta x/\Delta t$ ratio. Keeping the value of τ constant, we represented the stability limits found in Fig. 6a. Both the dimensional and conventional LBM presented the same $|\mathbf{u}|^{\max}$ values for the entire range of tested $\Delta x/\Delta t$. Our analysis revealed a linear relationship

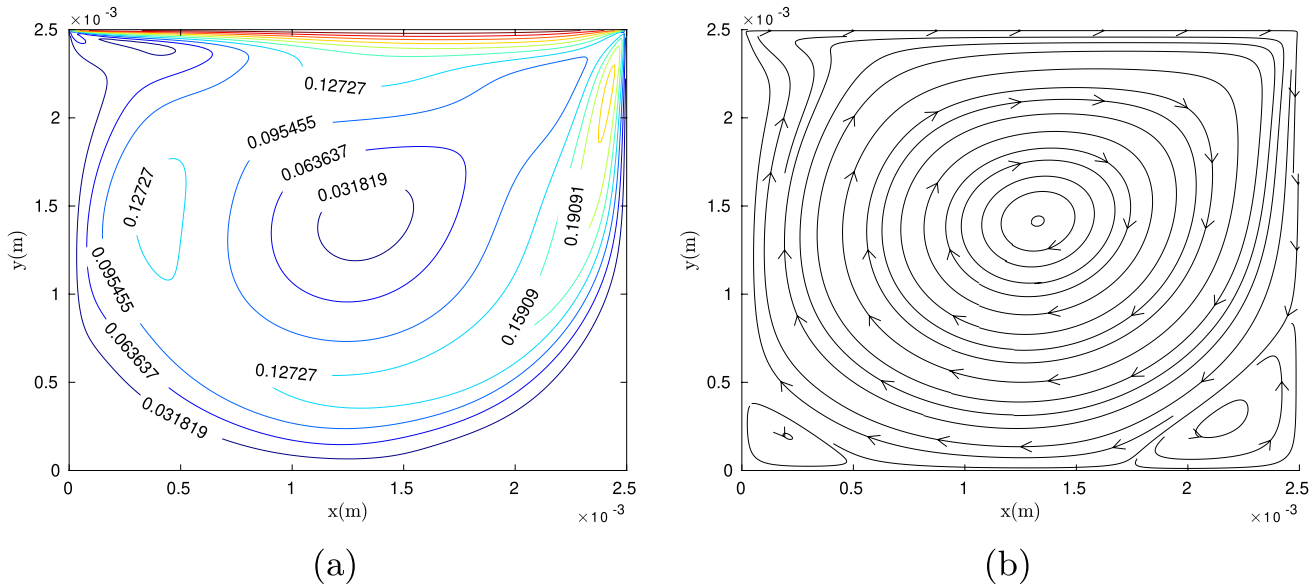

Fig. 4 **a** Speed contours (in ms^{-1}) and **b** streamlines for the dimensional LBM, considering the lid-driven cavity problem for $\text{Re} = 1000$

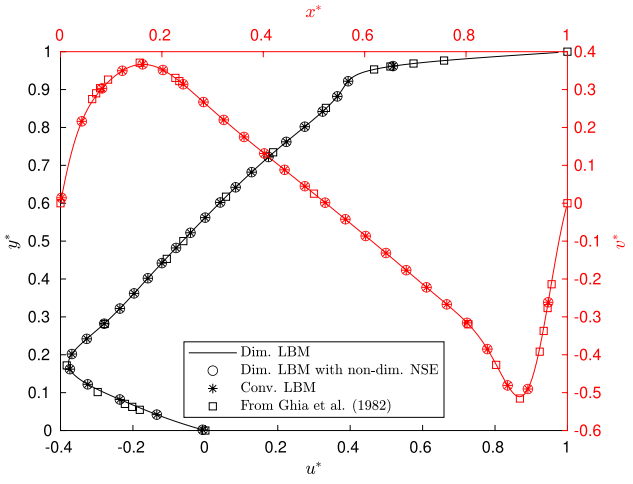

Fig. 5 Comparison between the results from dimensional LBM, from dimensional LBM with the non-dimensional NSE and traditional LBM, having as reference the results from Ghia et al. [21] for Re = 1000

between Δt and Δx values, dictated by the $|\mathbf{u}|^{\max}$ limitation: $\Delta x \geq 0.64225\Delta t$.

Additionally, we conducted a stability analysis to determine the stability region in Δt:Δx chart. This region is depicted in Fig. 6b, revealing that both the dimensional and conventional LBM models exhibit the same stability. Based on these results, we can conclude that the dimensional LBM will demonstrate the same stability outcomes as the conventional LBM, given that both employ the same discrete equations.

3.3 Heated channel

The third problem involves simulating forced convection in a two-dimensional channel (2D). The channel consists of two parallel plates subjected to external heat fluxes. This case was inspired by a problem from Nellis and Klein [61], problem 5–11, and we addressed it here due to its relevance in engineering, particularly in applications such as heat exchangers, electronic cooling microchannels and microfluidics. Also, it involves simulating a forced convection problem where we utilize the LBM to simulate both fluid flow and energy conservation. We employ the models presented in Sects. 2.1 and 2.2, respectively.

In this problem, we considered three different cases of forced convection between parallel plates. The first case involves simulating a fluid flow both thermally and hydrodynamically developed flow at the entrance of the channel, which is then subjected to alternating heat fluxes at the top and bottom boundaries. In the second case, we analyze a developing flow (both thermally and hydrodynamically) under a constant heat flux applied to both walls. The last scenario involves a developing flow with alternating heat fluxes at the walls. We analyzed the results of simulations for all three cases at the steady-state regime.

The geometry of the channel is $H : L = 0.0005$ m:0.010 m, where H and L represent the channel height and length, respectively. The fluid used is water, characterized by constant properties calculated at the mean temperature of 301 K, as summarized in Table 1. For this case, we considered the following BC: an imposed heat flux at the bottom and top walls (Neumman BC), a constant temperature inflow BC at

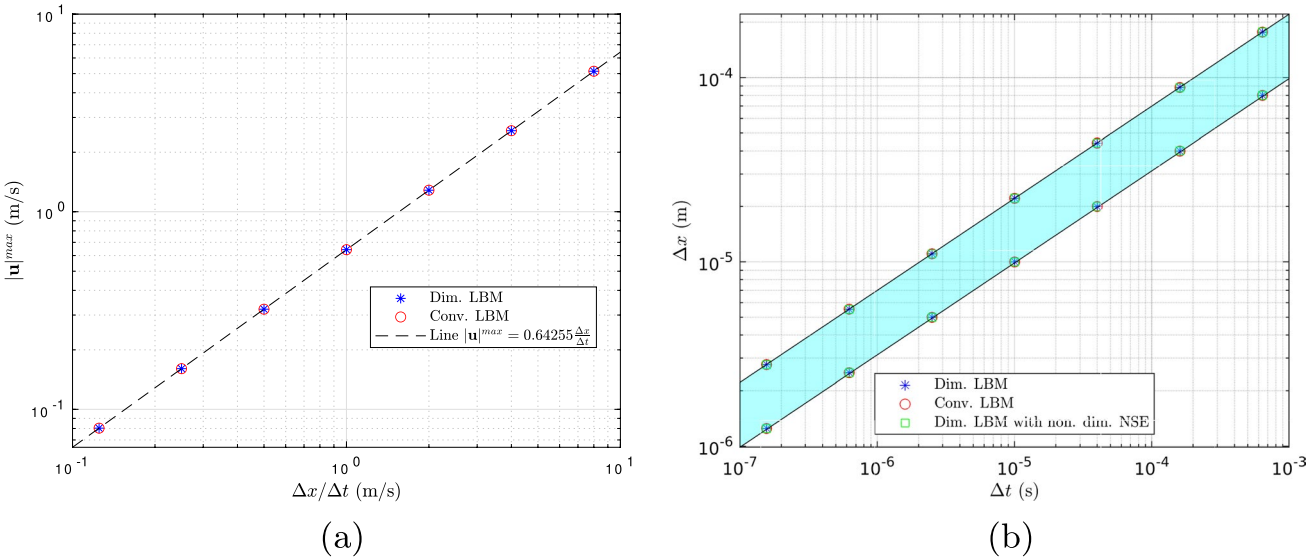

Fig. 6 **a** Maximum velocity modulus $|\mathbf{u}|^{\max}$ for distinct values of grid velocity $\Delta x/\Delta t$. **b** Stability map for the lid-driven cavity problem

Table 1 Thermodynamic and transport properties of water at 301 K and 1 atm, calculated from Bell et al. [5], used for the simulation of the forced convection in the heated channel

ρ	996.279 kg m^{-3}
ν	8.382e−7 m^{2}s^{-1}
k	0.611 W m^{-1}K^{-1}
c_p	4180.333 J kg^{-1}K$^{-1}\cdot$ m^{-3}
α	1.467e−7 m^{2}s^{-1}

the left boundary and an outflow BC at atmospheric pressure at the right wall.

We implemented the LBM boundary conditions with the following considerations. For the fluid flow aspect, we employed Eq. 14 for both inlet and stationary walls. The outlet BC was modeled using Eq. 14, as the channel is open to atmospheric pressure. For the simulation of the temperature field, we implemented the imposed heat flux on the bottom wall using Eq. 21, while the inlet BC was modeled using Eq. 20. At the outlet, we applied the first-order extrapolation scheme, as explained in Sect. 2.2. Due to channel's symmetry about its horizontal center line (with heat flux applied to both walls), we simulated only half of the domain ($H/2$), applying a symmetric BC for the top wall (resting at the y-center of the channel), as detailed in Sect. 2.1. For the analysis of results, the solution is mirrored to account for the entire channel.

In all the LBM simulations (for both models), we employed the $D2Q9$ velocity scheme, utilizing the BGK collision operator for fluid flow and the MRT for temperature field simulation. The MRT approach was necessary for solving the energy conservation equation due to stability and accuracy issues associated with the simulation of the developing flow.

For the first case, we assumed that water enters the channel with both thermally and hydrodynamically developed conditions. The velocity profile at the inlet is modeled by Eq. 44, where $u_m = 0.2$ m s^{-1} represents the mean velocity of the fluid. The temperature profile in this inlet region is described by Eq. 45, with $T_{\text{in}} = 300$ K as the mean temperature at the inlet. The y-axes represents the direction along the channel height, varying from the bottom to the top plate as $0 \leq y \leq H$. The x-axes points into the direction of the channel length, varying from $0 \leq x \leq L$, from the channel inlet to outlet.

$$u(y) = 6u_m\left(\frac{y}{H} - \frac{y^2}{H^2}\right) \tag{44}$$

$$T(y) = T_{\text{in}} + \frac{q_s'' H}{k}\left[-\left(\frac{y}{H}\right)^4 + 2\left(\frac{y}{H}\right)^3 - \frac{y}{H} + 0.243\right] \tag{45}$$

It is assumed that both plates are subjected to a periodic heat flux described by Eq. 46. The mean heat flux is maintained at $q_s'' = 40000$ W m^{-2}, with a variation about $\Delta q_s'' = 40000$ W m^{-2}, occurring at intervals of $L_h = 1$ mm. The signal function in the heat flux definition (sign) returns $+1$ if the argument is positive and -1, if it is negative.

$$q''(x) = q_s'' + \Delta q_s'' \text{ sign}\left[\sin\left(\frac{2\pi x}{L_h}\right)\right] \tag{46}$$

Given the conditions of the problem, the macroscopic equation describing the energy conservation for the first case is provided by Eq. 47. This equation was once again solved using a FD scheme to serve as a reference solution. The FD solution was obtained following the procedure outlined in Nellis and Klein [61], with $\Delta x_{\text{FDM}} = \Delta y_{\text{FDM}} = 1.25 \cdot 10^{-6}$ m for the entire channel, without applying symmetry BC.

$$u\frac{\partial T}{\partial x} = \alpha\left(\frac{\partial^2 T}{\partial x^2} + \frac{\partial^2 T}{\partial y^2}\right) \tag{47}$$

The numerical solutions are shown in Fig. 7. For both LBM models, we used a spatial grid interval of $\Delta x = 5.0 \cdot 10^{-6}$ m and a time step of $\Delta t = 2.0 \cdot 10^{-6}$ s. The LBM solutions correspond to the transient version of Eq. 47. The results depicted in Fig. 7a demonstrated excellent agreement between the LBM results, as well as between the LBM and FD solutions. The global errors measured for the LBM models, using the FD solution as reference, were $E_2^{\text{dim}} = 0.010\%$ and $E_2^{\text{conv}} = 0.012\%$, indicating very good agreement, with slightly smaller error for the dimensional LBM. Overall, the water temperature increases along its flow through the channel and exhibits oscillations in the heights near the heat flux sources.

In Fig. 7b, we show the variation of the local Nusselt number, Nu, with x for the dimensional LBM. Nu varies periodically with x, showing the same variation for each period of oscillation because the flow is completely developed. In this case, the average Nusselt number is equal to $\overline{\text{Nu}} = 6.67$.

In the second case, we considered a developing water flow in the same channel under a constant heat flux. Now, the water enters with a uniform velocity and temperature of $u_m = 0.02$ m s^{-1} and $T_{\text{in}} = 300$ K, respectively. The fluid is the channel is subjected to a uniform heat flux of $q'' = 40{,}000$ W m^{-2}. Treating of a developing flow problem, there are more changes in the velocity and temperature fields. Thus, we used lower values for the discrete time and space interval, about $\Delta x = 2.50 \cdot 10^{-6}$ m and $\Delta t = 6.25 \cdot 10^{-7}$ s, in order to obtain a convergent solution.

The temperature and velocity profiles given by the dimensional LBM for several cross-sections along the channel are shown in Fig. 8. We can observe that after a certain length along the channel, the velocity profile remains unchanged, indicating that the flow is hydrodynamically developed. For flow between parallel plates at low Reynolds numbers and a uniform profile at the inlet,

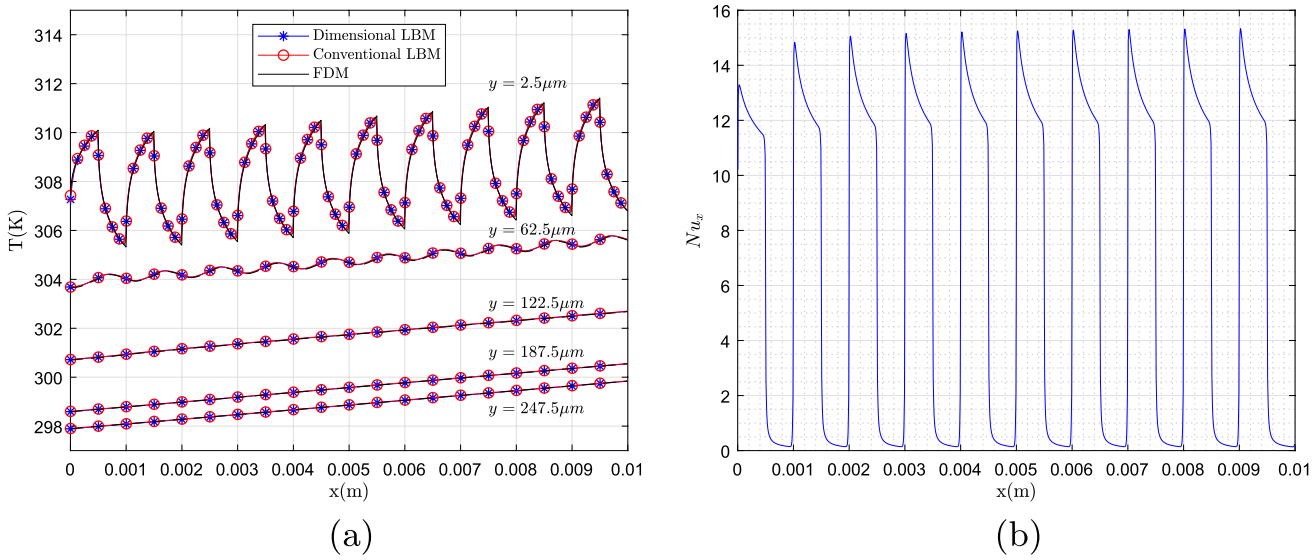

Fig. 7 **a** Temperature variation along the channel X-direction for several Y-values, obtained with the FDM and the conventional and dimensional LBM. **b** Local Nusselt number at the channel walls for the dimensional LBM simulation

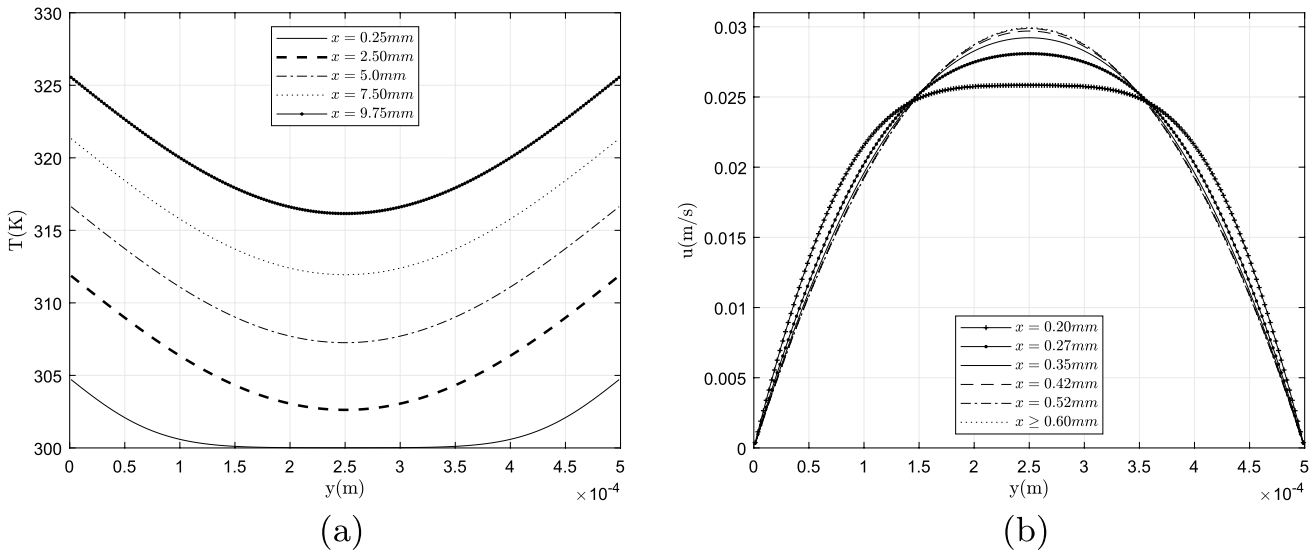

Fig. 8 Temperature (**a**) and velocity (**b**) *Y*-profiles at several cross-sections along the channel length for the developing flow

the hydrodynamic entrance length can be calculated as $L_e = D_h(0.3125 + 0.011\mathrm{Re}_D)$ [1]. In this case, with a channel Reynolds number of $\mathrm{Re}_D = 23.86$, the predicted hydrodynamic entrance length is $L_e = 0.57$ mm, while the length measured from the LBM results is approximately $L_e \approx 0.60$ mm. This result from simulations is consistent with the expectation from the analyzed relation. It should be noted that these relations are theoretical estimations. Additionally, it is known that the developed velocity profile must follow the analytical relation given by Eq. 44. Comparing the profile for $x = 0.60$ mm with the analytical velocity profile, we found a global error of about $E_2 = 0.1575\%$ for both conventional and dimensional LBM.

Similarly, at certain X-values, the temperature in the Y-direction case to vary in shape, increasing only in magnitude as the channel is heated, while maintaining the same ΔT in y. From this observation, and noting that the local Nusselt values do not change after approximately $x = 2.5$ mm (see Fig. 9b), we conclude that the channel length is sufficient for both the velocity and thermal profiles to become fully developed. Therefore, we can compare the developed value of the local Nusselt number with the expected value from the literature. For a developed flow between two parallel plates

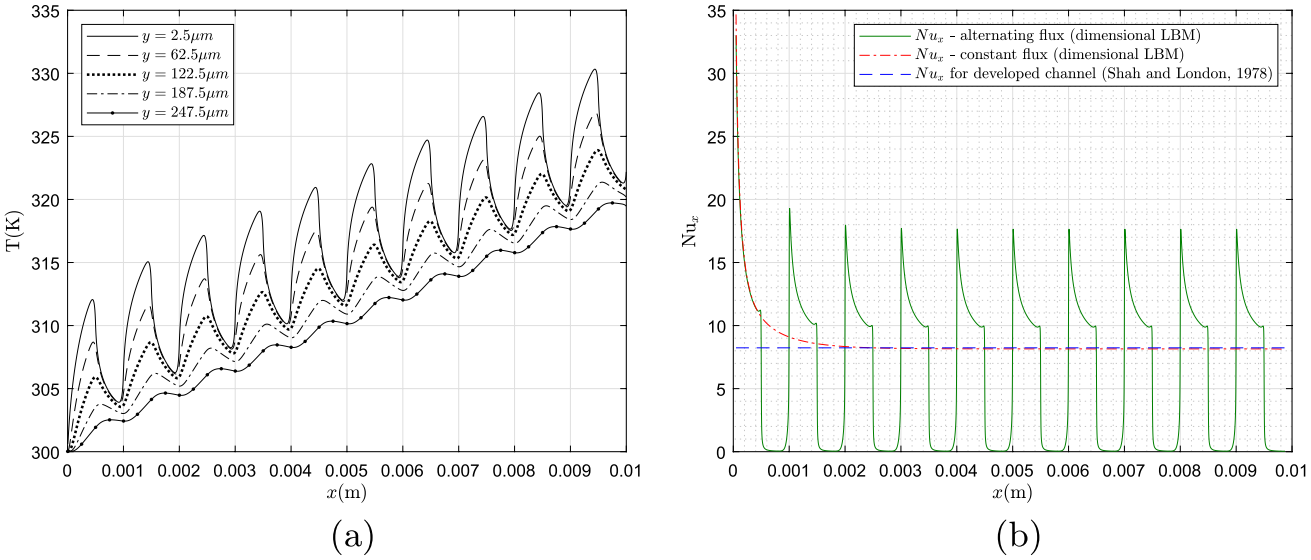

Fig. 9 **a** Temperature profiles along the x-direction at several Y-values for the developing flow with oscillating heat flux. **b** Local Nusselt number for the developing flow, considering both constant and oscillating heat flux and for the developed flow according to [70]

with constant and equal heat fluxes, the Nusselt number is Nu = 8.24 [70]. In the results provided by the dimensional LBM, we obtained $\mathrm{Nu}_{\mathrm{LBM}} = 8.15$, resulting in a very good agreement—a relative error of 1, 02%. The variation of the local Nusselt number on the channel walls is presented in Fig. 9b.

In the last case, the developing channel flow is subjected to an alternating heat flux given by Eq. 46, in order to compare the impact of this BC variation on the local Nusselt number. The spatial and time intervals used were the same as for the previous simulation ($\Delta x = 2.50 \cdot 10^{-6}$ m and $\Delta t = 6.25 \cdot 10^{-7}$ s). The steady-state temperature profiles obtained for this case are shown in Fig. 9a. As the flow is developing, we can observe a higher influence of the varying heat flux at the walls on the temperature profiles. As shown in Fig. 9b, the Nusselt number of the developing channel flow subjected to an alternating heat flux reaches higher local values than for the channel under a constant heat flux. However, the average Nusselt number was $\overline{\mathrm{Nu}}_{\mathrm{const}} = 8.92$ for the constant heat flux and $\overline{\mathrm{Nu}}_{\mathrm{var}} = 6.43$ for the varying one, the later being lower than the former due to the intermittency of the wall heat flux.

The temperature field along the entire channel is depicted in Fig. 10 for the three simulated cases, revealing several notable differences. In Fig. 10a, where the flow is fully developed at the channel inlet, the temperature distribution shows slight variations along the channel due to the heating process under the oscillating heat flux. In this case, the warmer fluid regions near the walls are slightly larger, and the cold fluid core decreases at the channel outlet. However, this is the only case where the temperature of the core fluid is almost equal to the smaller input temperature value. The other two cases involve developing flow under the constant and oscillating heat flux, Fig. 10b, c, respectively. In the case of the constant heat flux, the outlet mean temperature higher due to the constant heating experienced along the channel. The temperature field follows a similar pattern for the the developing flow subjected to an oscillating heat flux, but the convective heat transfer into the center of the channel is less pronounced due to the intermittency of the heat flux.

The higher average Nusselt number was obtained for the developing flow under a constant heat flux ($\overline{\mathrm{Nu}} = 8.92$). This value is even higher than the theoretical one for developed flow, Nu = 8.24, due to the effect of the development of the hydrodynamic and thermal boundary layers. For the two cases with oscillating heat flux, the average Nusselt numbers were lower, with values of $\overline{\mathrm{Nu}} = 6.67$ and $\overline{\mathrm{Nu}} = 6.43$ for the developed and developing flow, respectively. In this case, the inlet cold flow developing region decreased the total heat transferred from the wall heaters. The present problem could mimic the heat transfer process in a refrigerating channel of electronic devices.

In addition, it is important to mention that viscous dissipation was neglected in all simulations in this section. We based this assumption on the small values of the Brinkman number, B_r (Eq. 48). The highest value obtained was approximately $B_r = 10^{-5}$, indicating that the contribution of heat dissipation due to viscous stress is insignificant for these cases and can be safely neglected.

$$B_r = \frac{\zeta u_m^2}{k(T_w - T_m)} \tag{48}$$

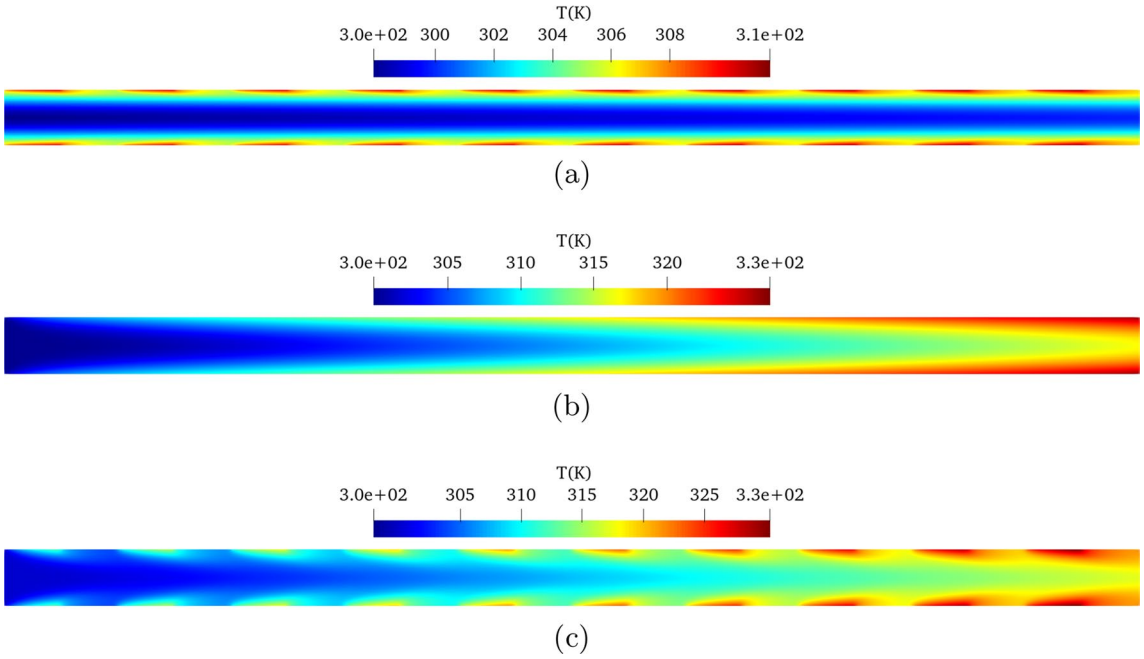

Fig. 10 Temperature field distribution along the channel, for the first (**a**), second (**b**) and third (**c**) simulated cases

In Appendices 1, 2 and 3, we showed simulation results obtained with the proposed dimensional LBM for other classical problems, including one-dimensional convection-diffusion flow, isothermal Pouseuille flow and natural convection in an enclosure. For the first two cases (Appendices 1 and 2), the obtained results are compared with analytical solutions. However, for natural convection (Appendix 3), the numerical solutions are compared against benchmark results available in the literature [14]. In all cases, the dimensional LBM results were also compared with conventional LBM results. All tests show very small global errors, indicating that the proposed LBM is physically coherent and accurate. Therefore, considering the results discussed in this section and those provided in Appendices 1, 2 and 3, we can conclude that the dimensional LBM is useful for simulating applied problems involving heat convection and diffusion.

For a final assessment of the thermal LBM, a stability analysis was conducted, considering both the dimensional and conventional approaches. Since we already demonstrated that both methods have the same stability for the momentum LBE (see Sect. 3.2), we focused on the hydrodynamic developed flow with alternating heat flux for this analysis. Given that the flow component is already at steady state, only the thermal LBE needs to be solved.

The stability map is depicted in Fig. 11. Once again, both LBM models exhibit the same stability regions. Interestingly, it appears that there is no lower limit as observed in Fig. 6. This is likely because we only solve the energy conservation LBE, without addressing the momentum LBE.

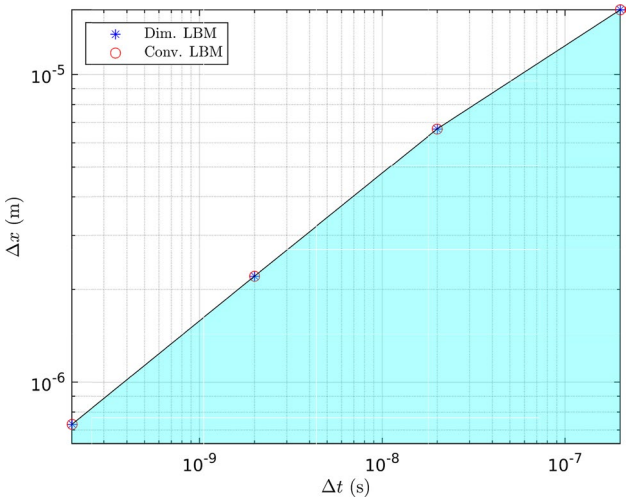

Fig. 11 Stability map for the forced convection in the hydrodynamic-developed thermal developing channel, considering both dimensional and conventional LBM

Consequently, the limit imposed by $|\mathbf{u}|^{\max}$ is absent, leaving only the diffusive limit related to τ_T.

3.4 Static bubble

In this section, we studied a two-phase fluid system consisting of one component (a liquid–vapor saturated water system) and two components (air–water system). Here, we considered the theoretical problem of a static bubble

surrounded by a liquid in equilibrium. This is a common benchmark test that allows for the evaluation of conventional and dimensional LBM performance.

The problem consists of a circular (2D) bubble with radius R surrounded by liquid, initialized at the center of a square domain. All the boundaries are considered periodic, and the order parameter ϕ (and consequently the density ρ) profile between the phases is initialized using Eq. 36 to avoid instabilities related to a sharp interface. As the system evolves over time, it reaches the equilibrium at the steady state, and the density profile must match the analytical solution represented by Eq. 49 [88]. Also, the relation between the pressure difference inside/outside the bubble ($\Delta P = P_{\text{out}} - P_{\text{in}}$) and the surface tension of the liquid σ follows the Laplace law, given by Eq. 50.

$$\rho(x,y) = \frac{(\rho_l + \rho_g)}{2} - \frac{(\rho_l - \rho_g)}{2} \tanh \left\{ \frac{2\left[\sqrt{(x-x_c)^2 + (y-y_c)^2} - R\right]}{W} \right\} \tag{49}$$

$$\Delta P = \frac{\sigma}{R} \tag{50}$$

We use the verification of these two relations to compare the performance of the dimensional LBM across four different two-phase systems. The first system is an air–water system at 25 °C and 101.325 kPa (1 atm). The other three systems consist of a vapor bubble surrounded by liquid phase of saturated water, without phase change, at three different saturated temperatures: 100 °C, 80 °C and 25 °C, respectively. The thermodynamic and transport properties for each system are presented in Table 2. To compare the dimensional and conventional LBM, we simulate the first system (water–air) with the both methods. The other three systems were only simulated using the dimensional LBM.

The domain has dimensions of 1 mm:1 mm, and for each system, we tested six different bubble radii: 0.250 mm, 0.225 mm, 0.20 mm, 0.175 mm, 0.150 mm and 0.125 mm. The interface width and mobility values were $W = 25.0 \cdot 10^{-6}$ m and $M = 1.0 \cdot 10^{-5}$ m^2 s^{-2}, respectively, and we selected discrete time and space intervals as $\Delta x = 5.0 \cdot 10^{-6}$ m and $\Delta t = 1.0 \cdot 10^{-7}$ s for all simulations. For the air–water system, the BGK collision operator was applied in all LBEs for both LBM models. In the case of the other three systems, the MRT operator was implemented for the two-phase momentum equation instead of Eq. 27, in order to achieve greater stability. We kept the BGK operator for the interface tracking LBE (Eq. 23).

A representation of the density contours for saturated water at 25 °C with a bubble of radius $R = 0.20$ mm is displayed Fig. 12a. In addition, the results for the density profile in the X-direction for the six tested bubble radii with saturated water at 25°C are presented in Fig. 12b. The global errors for the density profile compared to the analytical solution are shown in Table 3 for the four two-phase systems. We observe that the errors are very low for all cases, indicating the high accuracy of both LBM models. For the air–water system, the dimensional and conventional LBMs exhibit the same errors, suggesting that the dimensional LBM does not affect the accuracy of the LBM for this problem.

It should be noted that the results presented in Fig. 12 and Table 3 for saturated water at 25°C were obtained for very high density and viscosity ratios, namely: ρ_l/ρ_g =43,349.0, $\nu_g/\nu_l = 470.9$, and $\zeta_l/\zeta_g = 91.8$, (see Table 2). These ratios are exceptionally high and are not fully simulated in the open literature, underscoring the precision and reliability of the proposed dimensional LBM.

Considering verification of the Laplace law, we calculated the pressure inside the bubble (P_{in}) as the average of all gas nodes (where $\phi = 0.0$). Similarly, we obtained the outside pressure (P_{out}) by averaging the fluid nodes' pressure (where $\phi = 1.0$). The results from LBM simulations, compared

Table 2 Thermodynamic and transport properties of the four fluid systems considered for the static bubble simulations, obtained from [5]

	Air and water—25°C, 1 atm	Sat. water—100°C	Sat. water—80°C	Sat. water—25°C
ρ_g (kg m^{-3})	1.184	0.598	0.294	0.023
ρ_l (kg m^{-3})	997.048	958.349	971.766	997.003
ρ_l/ρ_g	842.1	1602.6	3305.3	43,349.0
ν_g (10^{-7}m^2 s^{-1})	155.770	204.493	392.919	4204.120
ν_l (10^{-7}m^2 s^{-1})	8.927	2.938	3.643	8.927
ν_g/ν_l	17.4	69.6	107.9	470.9
ζ_g (10^{-5}Pa s)	1.845	1.223	1.154	0.970
ζ_l (10^{-5}Pa s)	89.006	28.158	35.404	89.004
ζ_l/ζ_g	48.2	23.0	30.7	91.8
σ (N m^{-1})	0.072	0.059	0.063	0.072

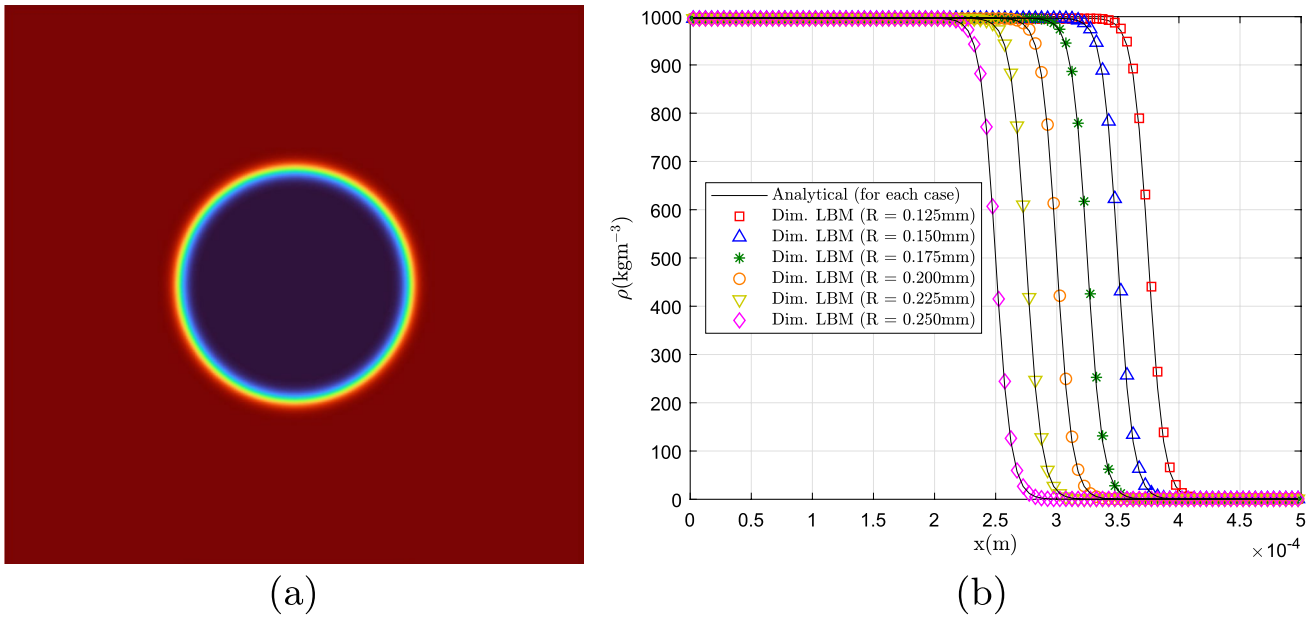

Fig. 12 **a** Representation of the density profiles for saturated water at 25°C, considering a bubble with radius $R = 0.20$ mm, being the blue region (inner part) occupied by the gas, and the red (outer part), by the liquid. **b** Density profiles at cross sections for each R value simulated, for the saturated water at 25 °C. (Obs: it was represented only a half of the cross-section, because the domain is symmetric) (color figure online)

Table 3 E_2 Results between LBM and analytical solutions of the density profiles for each value of R^{-1}

R^{-1} (m^{-1})	Air-water—25°C, 1 atm Dim. and Conv. LBM (%)	Sat. water—100°C (%)	Sat. water - 80°C (%)	Sat. water—25°C (%)
4000.0	0.253	0.253	0.253	0.253
4444.44	0.289	0.286	0.286	0.286
5000.0	0.316	0.316	0.316	0.316
5714.29	0.346	0.346	0.347	0.347
6666.67	0.391	0.392	0.392	0.392
8000.0	0.460	0.462	0.462	0.461

with the expected values from the Laplace law, are shown in Fig. 13, while the relative errors for each simulation are displayed in Table 4. Once again, we observe that the errors were the same for both the dimensional and conventional LBM in the case of the air–water system, as expected. Additionally, although greater than those for the density profiles, the errors observed for ΔP are considerable low. This validates all the simulated results and underscores the capability of the multiphase LBM presented in this work to accurately simulate real fluids with high density and viscosity ratios.

An important consideration is how the literature handles the relationship between the parameters of the physical system and their counterparts in lattice space. Commonly, traditional LBM is utilized for a set of dimensionless numbers and properties ratios. In simulations of the static bubble test found in the open literature, authors commonly aim to simulate a density ratio of $\rho_l/\rho_g = 1000$, often justifying that it approximates the water–air system. However, it is common for the viscosity ratios and surface tension employed in these simulations not to precisely correspond to the physical values of the system.

In the present simulations of the air–water system at 25°C, following the non-dimensionalization process explained previously, the following dimensionless parameters were utilized: $\tilde{\nu}_g = 1.682$, $\tilde{\nu}_l = 3.57 \cdot 10^{-3}$, $\tilde{\sigma} = 5.7648$, $\tilde{\rho}_g = 1.184$, $\tilde{\rho}_l = 997.084$ and $\tilde{M} = 0.040$. Notably, the dimensionless surface tension value in this problem, $\tilde{\sigma} = 5.7648$, exceeds the commonly used range, typically between 0.0001 and 0.2 [25, 26, 52, 53]. This "high" non-dimensional value is necessary to maintain the correct correspondence with the physical value of $\sigma = 0.072$ N m^{-1}. It underscores the importance of employing the LBM while considering the real physical properties of the systems, allowing for the study of method limitations and advantages from a more realistic perspective. This is the primary objective of the dimensional LBM proposition, where real physical conditions are automatically taken into account. The challenges now revolve around obtaining converged solutions, similar to any other traditional explicit method.

Ultimately, we conducted a numerical stability analysis for the air–water system, considering both LBM models, similar to the tests in Sects. 3.2 and 3.3. The stability map is depicted in Fig. 14. From this figure, we can conclude that,

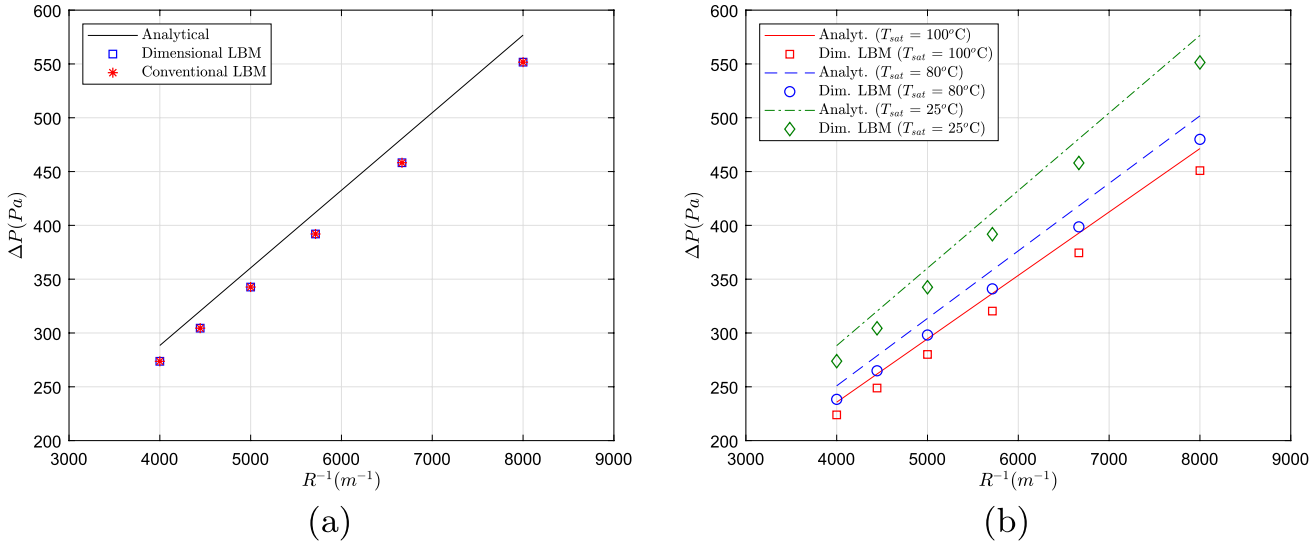

Fig. 13 **a** Pressure difference variation with R^{-1} obtained from the Laplace law and the conventional and dimensional LBM simulations for: **a** Air–water system and **b** saturated water systems

Table 4 E_2 Results between the LBM models simulations and the Laplace law for the pressure difference in the static bubble problem

R^{-1} (m^{-1})	Air-water—25°C, 1 atm Dim. and Conv. LBM (%)	Sat. water—100°C (%)	Sat. water—80°C (%)	Sat. water—25°C (%)
4000.0	5.097	4.998	4.998	4.996
4444.44	4.981	4.976	4.976	4.965
5000.0	4.943	4.936	4.936	4.935
5714.29	4.857	4.853	4.849	4.850
6666.67	4.675	4.667	4.666	4.667
8000.0	4.357	4.349	4.349	4.351

for the multiphase LBM model presented in Sect. 2.3, both methods exhibit the same stability.

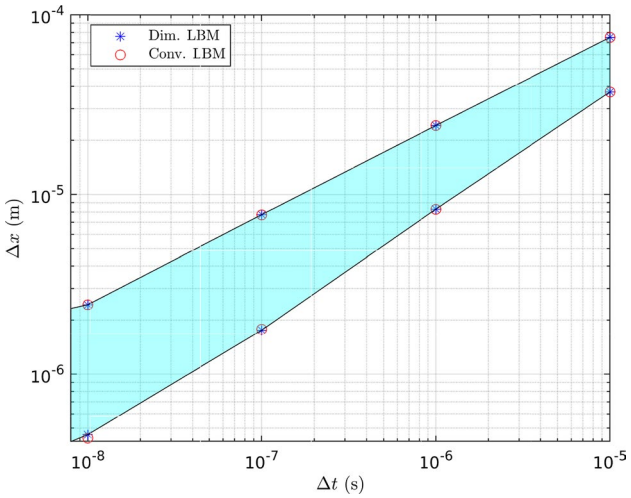

Fig. 14 Stability map for the static bubble simulation with the air–water system, considering both dimensional and conventional LBM

3.5 Layered Poiseuille flow

In this final section, we conduct a dynamic multiphase test to evaluate the performance of the dimensional LBM. This test involves a layered Poiseuille flow, which is a flow between two parallel plates where one phase occupies the lower half-part of the channel and the other phase occupies the upper half. The fluid is then subjected to a constant force field that accelerates both phases in the lengthwise direction of the channel. Upon reaching equilibrium between viscous forces and the force field, the system achieves a steady state with a constant velocity profile in the X-direction. It is important to mention that we have neglected any disturbance/oscillation of the interface, considering it as a perfect horizontal region.

We studied the stationary solution of the problem, assuming that the dynamic viscosity varies with the position y of the channel height in the same manner as the density. Adhering to the diffuse interface model followed by the LBM, we can simplify the NSE to obtain Eq. 51. The profile assumed for the dynamic viscosity is provided by Eq. 52. To obtain a reference solution, we solved the problem using a central second-order FD scheme.

It is important to note that if we were to consider a sharp interface between the phases, the problem would have an analytical solution [51, 64]. However, for coherence in the comparisons between the LBM models and the reference solution, we preferred to use the FD scheme described

previously. This scheme allows the consideration of a diffuse interface, represented by Eq. 52, consistent with the assumptions of the multiphase LBM model. Other authors in the literature have also made similar choices [18, 85]. The spatial interval used for the FD scheme was $\Delta y_{\mathrm{FDM}} = 4.0 \cdot 10^{-8}$ m, chosen to meet the convergence criteria established for the FD solutions at the beginning of the section.

$$\frac{\mathrm{d}}{\mathrm{dy}}\left[\zeta(y)\frac{\mathrm{d}u(y)}{\mathrm{dy}}\right] + F_x = 0 \tag{51}$$

$$\zeta(y) = \frac{(\zeta_l + \zeta_g)}{2} - \frac{(\zeta_l - \zeta_g)}{2}\tanh\left(\frac{2y - H}{W}\right) \tag{52}$$

Here, we considered the same four two-phase systems as in Sect. 3.4, applying both LBM models only to the air–water system. For the other three cases, which are saturated water systems at different temperatures (100°C, 80°C and 25°C), we only simulated using the dimensional LBM. The channel height was set to $H = 0.50$ mm, and since the steady-state solution does not depend on the channel length, we assumed a total channel length of $10\Delta x$ to reduce the simulation time. For LBM simulations, we used the $D2Q9$ velocity scheme with the BKG collision operator for the interface tracking equation (Eq. 23) and the MRT for the momentum equation. The interface width and the mobility were again assumed to be $W = 25.0 \cdot 10^{-6}$ m and $M = 1.0 \cdot 10^{-5}$ m^2 s^{-1}. For all simulations, the selected spatial and temporal discretization intervals were $\Delta x = 1.25 \cdot 10^{-6}$ m and $\Delta t = 1.25 \cdot 10^{-8}$ s. We took the driving force of the problem as $F_x = u_c(\zeta_l + \zeta_g)/H^2$, where $u_c = 1.0 \cdot 10^{-4}$ m s^{-1} represent the velocity at the center of the channel.

Furthermore, instead of using the linear relation between $\nu(\mathbf{x})$ and $\phi(\mathbf{x})$ as mentioned previously in Sect. 2.3, we now calculate the kinematic viscosity by the dynamic viscosity as $\nu(\mathbf{x}) = \zeta(\mathbf{x})/\rho(\mathbf{x})$, where $\zeta(\mathbf{x}) = \phi(\mathbf{x})(\zeta_l - \zeta_g) + \zeta_g$. This adjustment was made to achieve better results for the transition in the τ value at the interface, as indicated by [89] and [18].

The numerical solutions obtained with the LBM models compared to the FD method are presented in Fig. 15, with their respective global errors provided in Table 5. Once again, both LBM models showed the same errors for the air–water system, indicating the physical coherence of the dimensional LBM. The dimensional LBM model also exhibited very good accuracy for the other three cases (the saturated water systems). It is interesting to observe that the highest global error was observed for the saturated water at 100°C, which has the smallest kinematic viscosity ($\nu_l = 2.938 \cdot 10^{-7}$m^2 s^{-1}). This behavior is attributed to the fact that low kinematic viscosities lead to low τ values, which may result in the amplification of small instabilities. Although this instabilities are not significant enough to affect the convergence, they do reduce the accuracy. In this case of almost pure shear flow, the magnitude of viscosity has greater influence on the simulation results than the density ratio. Indeed, the global error for the saturated water at 25°C is the smallest among the saturated water systems, despite having the highest density ratio, equal to $\rho_l/\rho_g = 43{,}349.0$.

Now, to demonstrate the facilities of the dimensional procedure in numerical simulations, we present a simple analysis of grid refinement considering the saturated water system at 25°C, as an example. Initially, we employed a grid with $\Delta x = 5.0 \cdot 10^{-6}$ m and $\Delta t = 1.0 \cdot 10^{-7}$ s. However, this mesh size yielded poor accuracy results, resulting in a global error of $E_2 = 16.132\%$ (see Fig. 16). Subsequently, we halved the mesh in an attempt to improve the solution. To comply with the LBM stability criteria, we also adjusted the Δt value, resulting in the new discrete intervals $\Delta x_{\mathrm{new}} = 2.50 \cdot 10^{-6}$ m and $\Delta t_{\mathrm{new}} = 0.25 \cdot 10^{-7}$ s. The global error for this refined mesh was reduced to approximately $E_2 = 3.804\%$. Following this step, we further refined the mesh size to $\Delta x_{\mathrm{new2}} = 1.25 \cdot 10^{-6}$ m and $\Delta t_{\mathrm{new2}} = 0.125 \cdot 10^{-7}$ s. With this finer mesh, the smallest error was obtained, equal to $E_2 = 1.628\%$, as expected.

We did not performed further mesh refinements because the obtained errors were already sufficient small, as shown in Table 5, and conducting finer mesh simulations would require more computational time. Therefore, we utilized the finest mesh size for all the remaining simulations. From the explanation provided above, it is clear that the proposed dimensional LBM completely eliminates the need for dimensionalization processes, focusing solely on setting appropriate spatial and temporal discretization intervals. The results obtained indicate that the multiphase LBM is also suitable for addressing dynamic two-phase problems, even with very high density and viscosity ratios, which are rarely encountered in the open literature.

4 Conclusions

We presented a new implementation methodology for the lattice Boltzmann method, which considers all variables in physical units instead of converting them to the lattice space, as usually. To validate and analyze the applicability of the proposed LBM, several common engineering problems were solved. They include: one-dimensional heat conduction with heat generation; two-dimensional lid-driven cavity flow; two-dimensional forced convection in a channel under both oscillating and constant heat flux (for both developed and developing flows); two-dimensional multiphase stationary bubble in a liquid phase and two-dimensional multiphase-layered Pouseuille flow, all considering real

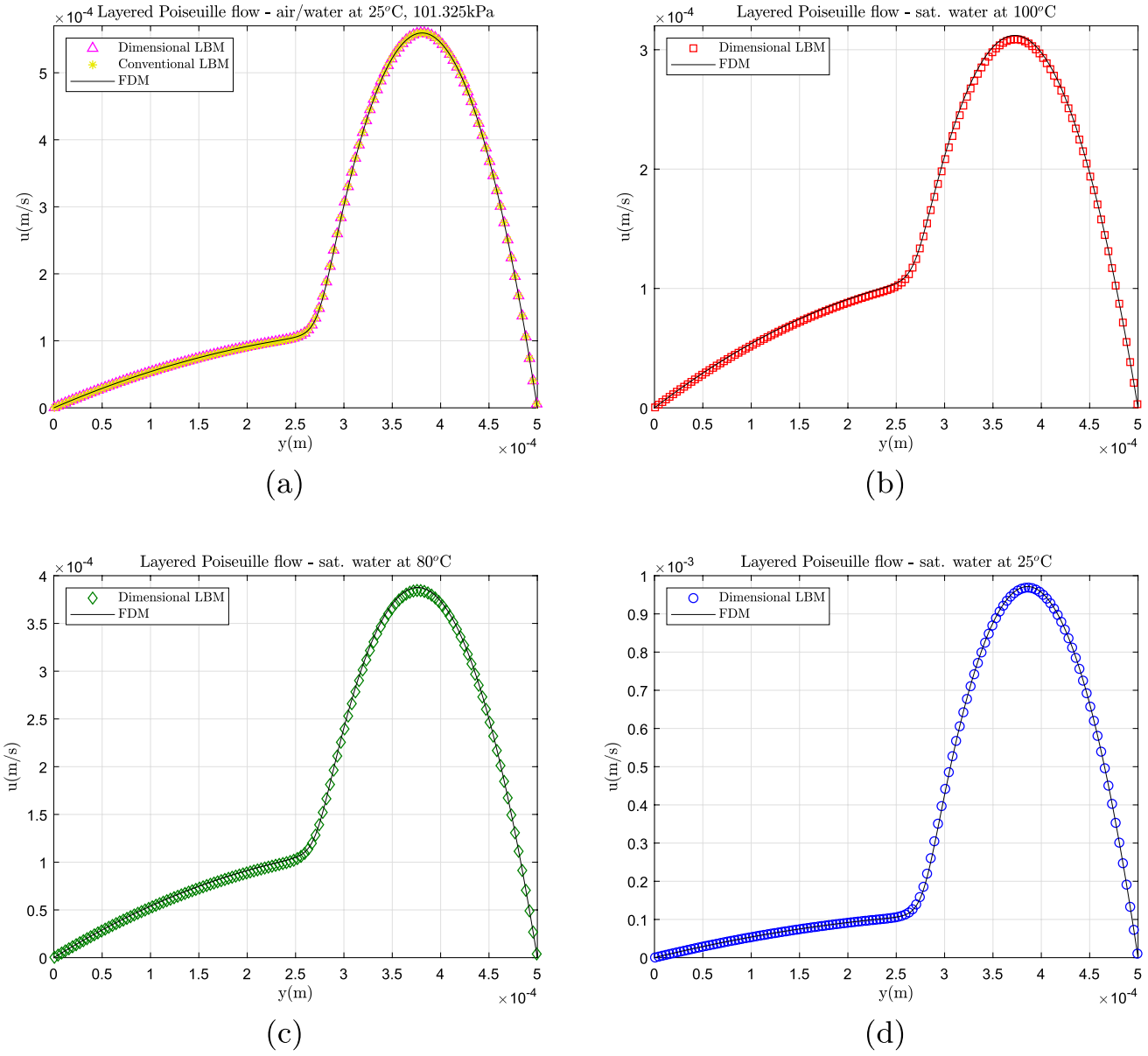

Fig. 15 Velocity profiles for the layered Poiseuille flow given by both LBM and FDM for: **a** air-water system, **b** saturated water at 100°C, **c** saturated water at 80°C and **d** saturated water at 25°C

Table 5 Global relative errors, E_2, between LBM simulations and FD solutions for the layered Poiseuille two-phase system cases

	Air-water—25°C, 1 atm both	Sat. water—100°C	Sat. water—80°C	Sat. water—25°C
$E_2(\%)$	0.282	1.628	1.311	0.817

fluids with very high density and viscosity ratios. Solutions for three additional problems, including: one-dimensional advection–diffusion equation, isothermal channel flow and natural convection, were briefly presented in Appendices 1, 2 and 3. All numerical results were compared with analytical solutions, when available, and with those provided by the FD scheme, otherwise. In all cases, the simulated results exhibited very good accuracy. The following main conclusions are provided.

I The obtained results confirm that the dimensional LBM can be safely used for simulating many common transport phenomena involving single-phase fluid flow and heat transfer processes, as well as hydrodynamic static and dynamic two-phase and two component flows. The proposed method pro-

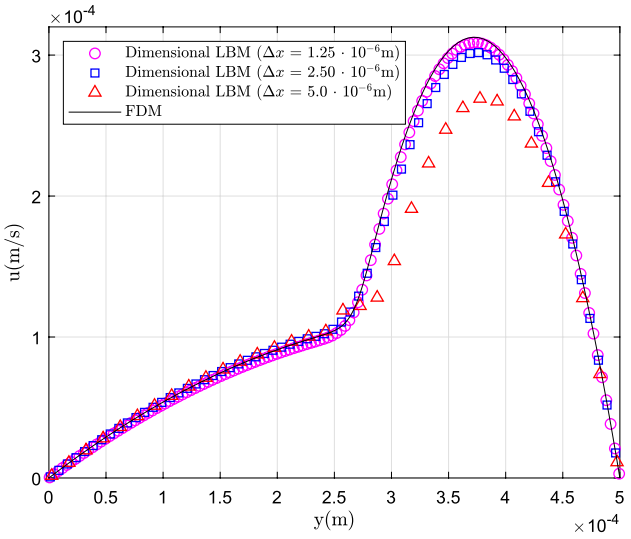

Fig. 16 Numerical solutions of the layered Poiseuille flow given by the dimensional LBM for the saturated water system at 100°C, considering three different spatial grids

duced accurate results, which were equal to those obtained with the conventional LBM for the same problems. Additionally, we verified that the dimensional LBM exhibits the same stability. The method can be extended to three dimensions and adapted for the use of other collision operators without major difficulties.

II Considering the discussed results, it is of paramount importance to highlight that in this work, we were able to simulate static and dynamic two-phase problems involving real fluids with high density and viscosity ratios. These rations reached values of $\rho_l/\rho_g = 43{,}300$ and $\nu_g/\nu_l = 470$, respectively, while maintaining good accuracy. To the best of authors' knowledge, these are novel findings of the phase-field multiphase lattice Boltzmann area, demonstrating the power of the LBM model described in Sect. 2.3, based on the use of Allen–Cahn equation. Additionally, these results underscore the facilities offered by the dimensional approach proposed in this paper.

III The use of the proposed dimensional LBM enables the development of numerical simulations for applied transport phenomena problems using physical units directly in all calculations. Indeed, the conversion to lattice units can make the application of the LBM more laborious, requiring additional steps for implementation. Therefore, the proposed method has the potential to enhance the use of LBM as simulation tool for a wide tange of problems in several fields.

IV The dimensional LBM can also be applied to solve non-dimensional problems when the governing equations are already non-dimensionalized, as explained in Sect. 2.5 and demonstrated in Sect. 3.2.

Appendix 1: 1D advection–diffusion equation

In this example, we solve the advection–diffusion equation in a 1D domain. Air at an average temperature of 335.50 K is considered, with the following properties: $\rho = 1.052$ kg m^{-3}, $c_p = 1008.174$ J kg^{-1}K^{-1} and $k = 0.029$ W m^{-1}K^{-1}. Initially, the domain is at $T_{\text{ini}} = 298.0$ K, and suddenly the right boundary is subjected to a temperature of $T_L = 373.0$ K, while the other end is maintained at $T_0 = 298.0$ K. The domain length is $L = 1.0$ m, and the air is moving with a constant speed $u = 0.001$ m s^{-1}.

The macroscopic equation that represents the physical problem is expressed by Eq. 53, and the corresponding analytical solution for the steady-state condition is given by Eq. 54.

$$u\frac{\partial T}{\partial x} = \alpha\frac{\partial^2 T}{\partial x^2} \tag{53}$$

$$T(x) = T_0 + (T_L - T_0)\left[\frac{\exp\left(\frac{\rho c_p u x}{k} - 1\right)}{\exp\left(\frac{\rho c_p u L}{k} - 1\right)}\right] \tag{54}$$

For this specific problem, given its simplicity in handling boundary conditions in the 1D case, we used the wet-node scheme for the boundaries instead of the link-wise scheme. This last scheme was used in the remainder of all simulations carried out in the paper. Then, using the $D1Q3$ velocity scheme, the BCs were implemented according to Eq. 55. Here, we considered the traditional BGK operator for the LBE, represented in Eq. 16.

$$\begin{cases} g_1(0, t+\Delta t) = T_0 - g_0(0, t+\Delta t) - g_2(0, t+\Delta t), & \text{for } x = 0.0; \\ g_2(L, t+\Delta t) = T_L - g_0(L, t+\Delta t) - g_1(L, t+\Delta t), & \text{for } x = L; \end{cases} \tag{55}$$

The LBM models are solved considering $\Delta x = 0.0125$ m and $\Delta t = 0.10$ s. The numerical solutions with LBM and the analytical solution are all shown in Fig. 17. Comparison of the solutions resulted in a global error of $E_2 = 0.030\%$ for both LBM models relative to the theoretical solution.

The results provided verify the accuracy of the dimensional LBM.

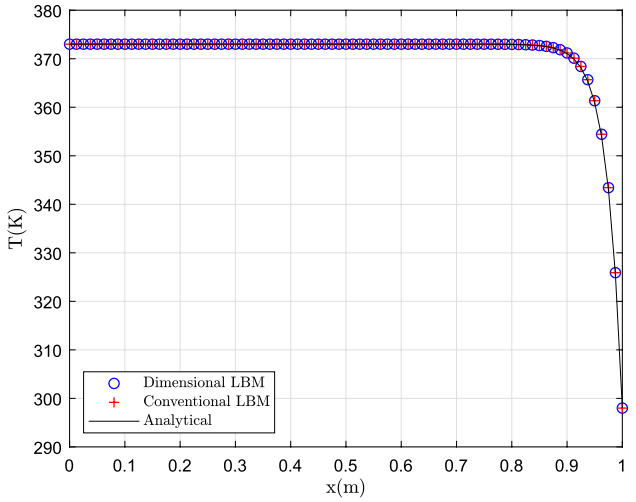

Fig. 17 Steady-state temperature distribution for the one-dimensional advection–diffusion problem

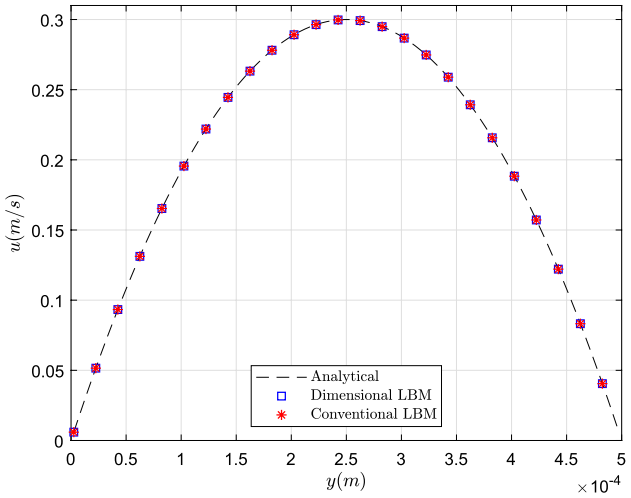

Fig. 18 Steady-state velocity profiles of the isothermal Poiseuille flow between two parallel plates obtained for the dimensional and conventional LBM simulations and the analytical solution

Appendix 2: isothermal channel flow

We also applied both LBM models to simulate an isothermal Poiseuille flow between two parallel plates. The distance between the plates was assumed to be $H = 0.50$ mm. As the analytical solution does not depend on the channel length (given by Eq. 44), we used 10 computational cells ($10\Delta x$) in the *X-direction*. We employed the $D2Q9$ velocity scheme with $\Delta x = 5.0 \cdot 10^{-6}$ m and $\Delta t = 1.0 \cdot 10^{-7}$ s.

The mean velocity of the channel was $u_m = 0.20m\ s^{-1}$ and the driving force in the x direction was $F_x = 12u_m\zeta/H^2$. The fluid is water at a mean temperature of 301 K, with properties listed in Table 1. The results are depicted in Fig. 18, and the global errors for both LBM models compared to the analytical solution are $E_2^{\text{dim}} = E_2^{\text{conv}} = 0.011\%$, indicating very good accuracy.

Appendix 3: natural convection in a square enclosure

In this Appendix, we simulate natural convection in a square enclosure with length $L = 0.0130$ m containing air initially at $T_{\text{ini}} = 293.85$ K. The left wall of the domain is maintained at a higher constant temperature equal to $T_h = 373.15$ K, while the right wall remains at the initial temperature of $T_c = 293.85$ K. The upper (top) and lower (bottom) walls are considered insulated. Air properties are calculated at a reference temperature of $T_{\text{ref}} = 333.50$ K: $\rho = 1.059\,\text{kg m}^{-3}, c_p = 1008.045\,\text{J kg}^{-1}\text{K}^{-1}, k = 0.029\,\text{W m}^{-1}\,\text{K}^{-1}$, $\alpha = 2.702 \cdot 10^{-5}$ m^2 s, $\nu = 1.90 \cdot 10^{-5}$ m^2 s and $\beta_{\text{exp}} = 3.004 \cdot 10^{-3}K^{-1}$ (thermal expansion coefficient).

The temperature difference between the walls causes a mass flux due to the difference in density between the hot and cold fluids. To consider this effect without changing the fluid density in the simulations, we assumed a buoyancy force given by Eq. 56 [57, 60, 77]. This is the so-called Boussinesq approximation. In this equation, $\overline{\rho}$ is the reference density, calculated at the reference temperature T_{ref}, and $\mathbf{g} = (0, -9.81)$ m s^{-2} is the gravitational acceleration.

$$\mathbf{F_b}(\mathbf{x}, t) = -\overline{\rho}\beta_{\text{exp}}\left[T(\mathbf{x}, t) - T_{\text{ref}}\right]\mathbf{g} \tag{56}$$

We considered the $D2Q9$ velocity set, with the BGK and MRT collision operators for momentum and thermal LBEs, respectively. For stationary walls, we used the bounce-back BC for the momentum distribution function (Eq. 13). Furthermore, for the fixed temperature BCs (left and right walls), we employed the anti-bounce-back rule (Eq. 20), and the upper and lower walls were modeled as thermally insulated, just applying the BB rule (Eq. 21) with zero heat flux ($q'' = 0$).

The problem can be characterized by the Rayleigh number (Eq. 57), which will be considered as $\text{Ra} = 10^4$ for the first case and $\text{Ra} = 10^6$, for the second. In this last test, to obtain $\text{Ra} = 10^6$ without changing the average fluid temperature, we considered a new square cavity size, equal to $L = 0.60$ m, and the wall temperatures were changed to $T_h = 373.85$ K and $T_c = 293.15$ K, keeping $T_{\text{ref}} = 333.50$ K. Therefore, the air properties in both tests were maintained constant and unchanged.

$$\text{Ra} = \frac{|\mathbf{g}|\beta_{\text{exp}}L^3(T_h - T_c)}{\nu\alpha} \tag{57}$$

Table 6 Calculated average Nusselt numbers from the simulated results by both LBM models and the benchmark solution [14]

	Ra = 10^4		Ra = 10^6	
	$\overline{\text{Nu}}$	Error (%)	$\overline{\text{Nu}}$	Error (%)
Benchmark [14]	2.243	–	8.800	–
Dim. LBM	2.242	0.045	8.805	0.057
Conv. LBM	2.242	0.045	8.794	0.068

For both cases, discrete space and time intervals equal to $\Delta x = 2.0 \cdot 10^{-4}$ m and $\Delta t = 2.0 \cdot 10^{-4}$ s, were considered, respectively. Steady-state results for the temperature contours and streamlines are presented in Figs. 19 and 20. To evaluate the dimensional LBM, its solution is compared with the results of the conventional LBM, and both numerical solutions are validated through a comparison with the benchmark solutions found in the literature [14]. All these

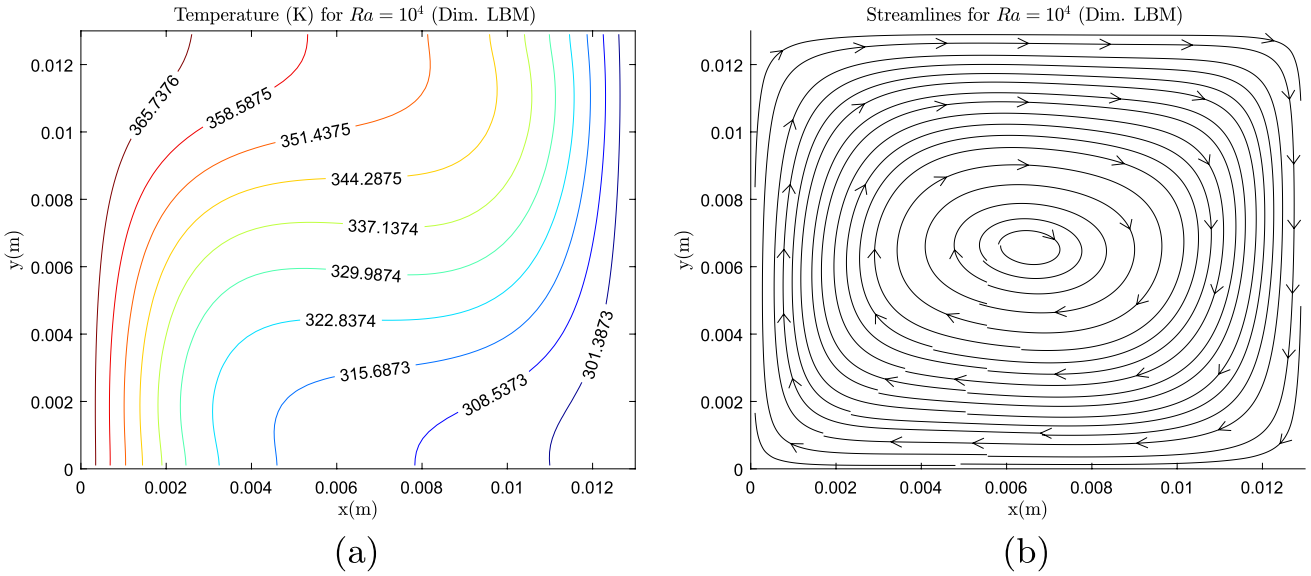

Fig. 19 Simulated temperature contours (**a**) and streamlines (**b**) for Ra = 10^4 with the dimensional LBM

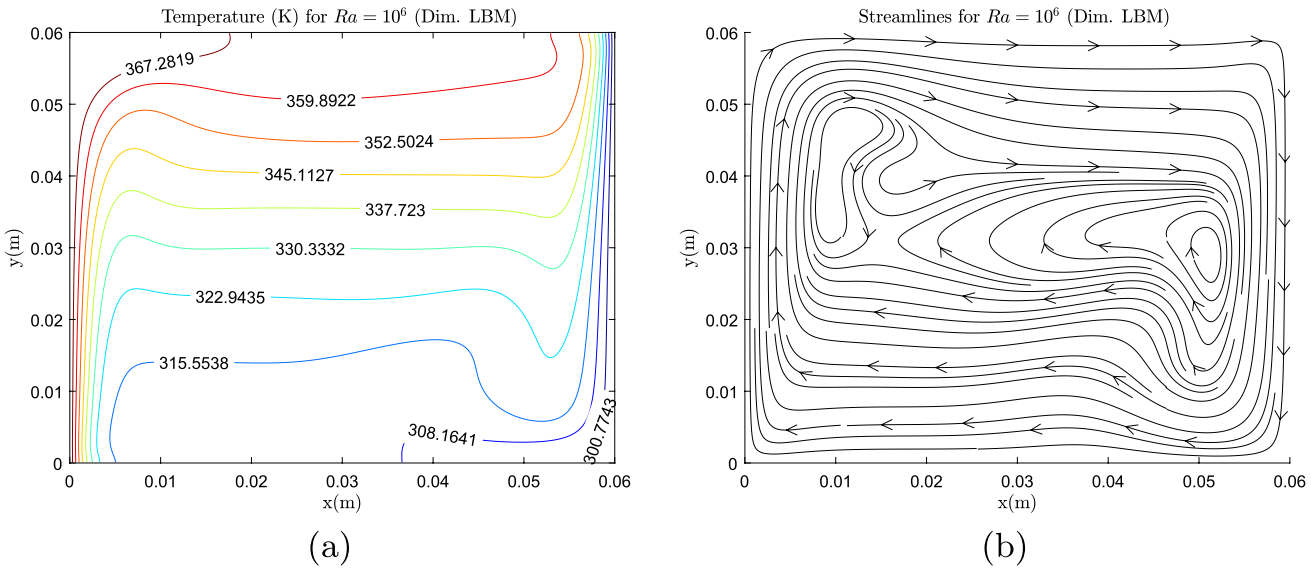

Fig. 20 Simulated temperature contours (**a**) and streamlines (**b**) for Ra = 10^6 with the dimensional LBM

solutions are presented in Table 6. Both LBM models showed good agreement with the benchmark expected values, presenting very small global errors, E_2.

Acknowledgements The authors acknowledge the support received from FAPESP (São Paulo Research Foundation, Grants 2023/02383-6, 2019/21022-9 and 2016/09509-1) and CNPq (National Council for Scientific and Technological Development, process 305941/2020-8).

References

1. Atkinson B, Brocklebank MP, Card CCH et al (1969) Low Reynolds number developing flows. AIChE J 15:548–553
2. Baakeem SS, Bawazeer SA, Mohamad AA (2021) A novel approach of unit conversion in the lattice Boltzmann method. Appl Sci 11:6386
3. Bakarji J, Callaham J, Brunton SL et al (2022) Dimensionally consistent learning with Buckingham Pi. Nat Comput Sci 2(12):834–844
4. Bawazeer SA, Baakeem SS, Mohamad AA (2021) A critical review of forcing schemes in lattice Boltzmann method: 1993–2019. Arch Comput Methods Eng 28:4405–4423
5. Bell IH, Wronski J, Quoilin S et al (2014) Pure and pseudo-pure fluid thermophysical property evaluation and the open-source thermophysical property library CoolProp. Ind Eng Chem Res 53(6):2498–2508
6. Bhatnagar PL, Gross EP, Krook M (1954) A model for collision processes in gases. I. Small amplitude processes in charged and neutral one-component systems. Phys Rev 94(3):511–525
7. Bray AJ (1994) Theory of phase ordering kinetics. Adv Phys 43(3):357–459
8. Buckingham E (1914) On physically similar systems; Illustrations of the use of dimensional equations. Phys Rev 4(4):345–376
9. Cates ME, Desplat JC, Stansell P et al (2005) Physical and computational scaling issues in lattice Boltzmann simulations of binary fluid mixtures. Philos Trans R Soc A 363:1917–1935
10. Chapman S, Cowling TG (1952) The mathematical theory of non-uniform gases, 2nd edn. Cambridge University Press, Cambridge
11. Chen Q, Zhang XB, Zhang JF (2014) Numerical simulation of Neumann boundary condition in the thermal lattice Boltzmann model. Int J Mod Phys C 25(8):1450027
12. Chen S, Doolen GD (1998) Lattice Boltzmann method for fluid flows. Annu Rev Fluid Mech 30(1):329–364
13. Chiu PH, Lin YT (2011) A conservative phase field method for solving incompressible two-phase flows. J Comput Phys 230:185–204
14. Davis GDV (1983) Natural convection of air in a square cavity: a bench mark numerical solution. Int J Numer Methods Fluids 3:249–264
15. de Fabritiis G, Mancini A, Mansutti D et al (1998) Mesoscopic models of liquid/solid phase transitions. Int J Mod Phys C 09(08):1405–1415
16. Fakhari A, Rahimian MH (2010) Phase-field modeling by the method of lattice Boltzmann equations. Phys Rev E 81:036707
17. Fakhari A, Geierb M, Lee T (2016) A mass-conserving lattice Boltzmann method with dynamic grid refinement for immiscible two-phase flows. J Comput Phys 315:434–457
18. Fakhari A, Mitchell T, Leonardi C et al (2017) Improved locality of the phase-field lattice Boltzmann model for immiscible fluids at high density ratios. Phys Rev E 96:053301
19. Fei L, Luo KH (2018) Cascaded lattice Boltzmann method for incompressible thermal flows with heat sources and general thermal boundary conditions. Comput Fluids 165:89–95
20. Ferziger JH, Peric M, Leonard A (2002) Computational methods for fluid dynamics, vol 50, 3rd edn. Springer, New York
21. Ghia U, Ghia K, Shin C (1982) High-Re solutions for incompressible flow using the Navier–Stokes equations and a multigrid method. J Comput Phys 48(3):387–411
22. Ginzburg I (2005) Generic boundary conditions for lattice Boltzmann models and their application to advection and anisotropic dispersion equations. Adv Water Resour 28:1196–1216
23. Guo Z, Shu C (2013) Lattice Boltzmann method and its applications in engineering. World Scientific Publishing Co. Pte. Ltd., Singapore
24. Guo Z, Zheng C, Shi B (2002) Discrete lattice effects on the forcing term in the lattice Boltzmann method. Phys Rev E 65:046308
25. Haghani-Hassan-Abadi R, Fakhari A, Rahimian MH (2021) Phase-change modeling based on a novel conservative phase-field method. J Comput Phys 432:110111
26. He Q, Li Y, Huang W et al (2019) Phase-field-based lattice Boltzmann model for liquid-gas-solid flow. Phys Rev E 100:033314
27. He X, Chen S, Doolen GD (1998) A novel thermal model for the lattice Boltzmann method in incompressible limit. J Comput Phys 146(1):282–300
28. He X, Chen S, Zhang R (1999) A lattice Boltzmann scheme for incompressible multiphase flow and its application in simulation of Rayleigh–Taylor instability. J Comput Phys 152:642–663
29. Higuera FJ, Jiménez J (1989) Boltzmann approach to lattice gas simulations. Europhys Lett 9(7):663
30. Huang H, Sukop MC, Lu XY (2015) Multiphase lattice Boltzmann methods: theory and applications. John Wiley & Sons Ltd., Hoboken
31. Huang J, Bao C, Jiang Z et al (2019) A general approach of unit conversion system in lattice Boltzmann method and applications for convective heat transfer in tube banks. Int J Heat Mass Transf 135:873–884
32. Inamuro T, Yoshino M, Suzuki K (2022) An introduction to the lattice Boltzmann method: a numerical method for complex boundary and moving boundary flows. World Scientific Publishing Co. Pte. Ltd., Singapore
33. Jacqmin D (1999) Calculation of two-phase Navier–Stokes flows using phase-field modeling. J Comput Phys 155:96–127
34. Jamet D, Lebaigue O, Coutris N et al (2001) The second gradient method for the direct numerical simulation of liquid-vapor flows with phase change. J Comput Phys 169:624–651
35. Jaramillo A, Mapelli VP, Cabezas-Gómez L (2022) Pseudopotential lattice Boltzmann method for boiling heat transfer: a mesh refinement procedure. Appl Therm Eng 213:118705
36. Kang Q, Zhang D, Chen S (2002) Unified lattice Boltzmann method for flow in multiscale porous media. Phys Rev E 66:056307
37. Khoshtarash H, Siavashi M, Ramezanpour M et al (2023) Pore-scale analysis of two-phase nanofluid flow and heat transfer in open-cell metal foams considering Brownian motion. Appl Therm Eng 221:119847
38. Krüger T, Kusumaatmaja H, Kuzmin A et al (2017) The lattice Boltzmann method: principles and practice. Springer International Publishing, Cham
39. Kuzmin A (2010) Multiphase simulations with lattice Boltzmann scheme. PhD thesis, University of Calgary
40. Kuzmin A, Guo ZL, Mohamad AA (2011) Simultaneous incorporation of mass and force terms in the multi-relaxation-time

framework for lattice Boltzmann schemes. Philos Trans R Soc 369:2219–2227
41. Ladd AJC (1994) Numerical simulations of particulate suspensions via a discretized Boltzmann equation. Part 1. Theoretical foundation. J Fluid Mech 271:285–309
42. Ladd AJC, Verberg R (2001) Lattice-Boltzmann simulations of particle-fluid suspensions. J Stat Phys 104(5–6):1191–1251
43. Lallemand P, Luo LS (2000) Theory of the lattice Boltzmann method: dispersion, dissipation, isotropy, Galilean invariance, and stability. Phys Rev E 61:65463
44. Lee T, Liu L (2010) Lattice Boltzmann simulations of micron-scale drop impact on dry surfaces. J Comput Phys 229:8045–8063
45. Li L, Mei R, Klausner JF (2013) Boundary conditions for thermal lattice Boltzmann equation method. J Comput Phys 237:366–395
46. Li L, Mei R, Klausner JF (2017) Lattice Boltzmann models for the convection–diffusion equation: D2Q5 vs D2Q9. Int J Heat Mass Transf 108:41–62
47. Li Q, Luo K, Kang Q et al (2016) Lattice Boltzmann methods for multiphase flow and phase-change heat transfer. Prog Energy Combust Sci 52(14):62–105
48. Li W, Li Q, Yu Y et al (2021) Nucleate boiling enhancement by structured surfaces with distributed wettability-modified regions: a lattice Boltzmann study. Appl Therm Eng 194:117130
49. Liang H, Shi BC, Guo ZL et al (2014) Phase-field-based multiple-relaxation-time lattice Boltzmann model for incompressible multiphase flows. Phys Rev E 89:053320
50. Liang H, Shi BC, Chai ZH (2016) Lattice Boltzmann modeling of three-phase incompressible flows. Phys Rev E 93:013308
51. Liang H, Shi BC, Chai ZH (2017) An efficient phase-field-based multiple-relaxation time lattice Boltzmann model for three-dimensional multiphase flows. Comput Math Appl 73:1524–1538
52. Liang H, Xu J, Chen J et al (2018) Phase-field-based lattice Boltzmann modeling of large-density-ratio two-phase flows. Phys Rev E 98:033301
53. Liang H, Liu H, Chai Z et al (2019) Lattice Boltzmann method for contact-line motion of binary fluids with high density ratio. Phys Rev E 99:063306
54. Liu Q, He YL, Li Q et al (2014) A multiple-relaxation-time lattice Boltzmann model for convection heat transfer in porous media. Int J Heat Mass Transf 73:761–775
55. Martins IT, Gómez LC (2022) Microchannel conjugate heat transfer modeling using lattice Boltzmann method with a new discretization strategy. J Enhanc Heat Transf 29(3):79–102
56. McNamara G, Zanetti G (1988) Use of the Boltzmann equation to simulate lattice-gas automata. Phys Rev Lett 61:2332–2335
57. Mezrhab A, Moussaoui MA, Jami M et al (2010) Double MRT thermal lattice Boltzmann method for simulating convective flows. Phys Lett A 374:3499–3507
58. Miller W, Succi S, Mansutti D (2001) Lattice Boltzmann model for anisotropic liquid-solid phase transition. Phys Rev Lett 86:3578–3581
59. Mohamad AA (2019) Lattice Boltzmann method: fundamentals and engineering applications with computer codes. Springer-Verlag London Ltd., London
60. Mohamad AA, Kuzmin A (2010) A critical evaluation of force term in lattice Boltzmann method, natural convection problem. Int J Heat Mass Transf 53:990–996
61. Nellis G, Klein S (2009) Heat transfer. Cambridge University Press, Cambridge
62. Qian YH, D'Humieres D, Lalleman P (1992) Lattice BGK models for Navier–Stokes equation. Europhys Lett 17(6):479–484
63. Reichl LE (1998) A modern course in statiscical physics, 2nd edn. John Wiley & Sons Inc., Hoboken
64. Ren F, Song B, Sukop MC et al (2016) Improved lattice Boltzmann modeling of binary flow based on the conservative Allen–Cahn equation. Phys Rev E 94:023311
65. Roache PJ (1998) Verification and validation in computational science and engineering, 1st edn. Hermosa Publishers, New Mexico
66. Rothman DH, Keller JM (1988) Immiscible cellular-automaton fluids. J Stat Phys 52:1119–1127
67. Rowlinson JS, Widom B (1982) Molecular theory of capillarity. Dover Publications Inc., Mineola
68. Safari H, Rahimian MH, Krafczyk M (2013) Extended lattice Boltzmann method for numerical simulation of thermal phase change in two-phase fluid flow. Phys Rev E 88:013304
69. Seta T (2013) Implicit temperature correction-based immersed boundary-thermal lattice Boltzmann method for the simulation of natural convection. Phys Rev E 87:063304
70. Shah RK, London AL (1978) Laminar flow forced convection in ducts. Academic Press, Cambridge
71. Shan X, Chen H (1993) Lattice Boltzmann model for simulating flows with multiple phases and components. Phys Rev E 47:1815–1819
72. Shan X, Chen H (1994) Simulation of nonideal gases and liquid-gas phase transitions by the lattice Boltzmann equation. Phys Rev E 49:2941–2948
73. Sheikholeslami M, Gorji-Bandpy M, Ganji D (2014) Lattice Boltzmann method for MHD natural convection heat transfer using nanofluid. Powder Technol 254:82–93
74. Su Y, Davidson JH (2016) A new mesoscopic scale timestep adjustable non-dimensional lattice Boltzmann method for melting and solidification heat transfer. Int J Heat Mass Transf 92:1106–1119
75. Succi S (2018) The lattice Boltzmann equation for complex states of flowing matter. Oxford University Press, Oxford
76. Swift MR, Orlandini E, Osborn WR et al (1996) Lattice Boltzmann simulations of liquid-gas and binary fluid systems. Phys Rev E 54:5041–5052
77. Wang J, Wang D, Lallemand P et al (2013) Lattice Boltzmann simulations of thermal convective flows in two dimensions. Comput Math Appl 65:262–286
78. Wang L, Zeng Z, Zhang L et al (2016) A lattice Boltzmann model for thermal flows through porous media. Appl Therm Eng 108:66–75
79. Wang SC, Tong ZX, He YL et al (2022) Unit conversion in pseudopotential lattice Boltzmann method for liquid-vapor phase change simulations. Phys Fluids 34:103305
80. Wolf-Gladrow DA (2000) Lattice-gas cellular automata and lattice Boltzmann models: an introduction. Springer, Berlin, Heidelberg
81. Wu F, Rao Z (2017) The lattice Boltzmann investigation of natural convection for nanofluid based battery thermal management. Appl Therm Eng 115:659–669
82. Xuan Y, Yao Z (2005) Lattice Boltzmann model for nanofluids. Heat Mass Transf 41:199–205
83. Yan Y, Zu Y, Dong B (2011) LBM, a useful tool for mesoscale modelling of single-phase and multiphase flow. Appl Therm Eng 31(5):649–655
84. Yoshida H, Nagaoka M (2010) Multiple-relaxation-time lattice Boltzmann model for the convection and anisotropic diffusion equation. J Comput Phys 229:7774–7795
85. Zhang S, Tang J, Wu H (2022) Phase-field lattice Boltzmann model for two-phase flows with large density ratio. Phys Rev E 105:015304
86. Zhang T, Shi B, Guo Z et al (2012) General bounce-back scheme for concentration boundary condition in the lattice-Boltzmann method. Phys Rev E 85:016701
87. Zheng HW, Shu C, Chew YT (2006) A lattice Boltzmann model for multiphase flows with large density ratio. J Comput Phys 218:353–371

88. Zu YQ, He S (2013) Phase-field-based lattice Boltzmann model for incompressible binary fluid systems with density and viscosity contrasts. Phys Rev E 87:043301
89. Zu YQ, He S (2013) Phase-field-based lattice Boltzmann model for incompressible binary fluid systems with density and viscosity contrasts. Phys Rev E 87:043301